
Article:
Metcalfe, G.D. orcid.org/0000-0001-7444-7137, Smith, T.W. and Hippler, M. orcid.org/0000-0002-3956-3922 (2021) Advanced spectroscopic analysis and 15N-isotopic labelling study of nitrate and nitrite reduction to ammonia and nitrous oxide by E. coli. Analyst, 146 (22). pp. 7021-7033. ISSN 0003-2654

https://doi.org/10.1039/d1an01261d

Analyst

ROYAL SOCIETY OF CHEMISTRY

PAPER

View Article Online
View Journal | View Issue

Cite this: *Analyst*, 2021, **146**, 7021

Advanced spectroscopic analysis and ^{15}N-isotopic labelling study of nitrate and nitrite reduction to ammonia and nitrous oxide by *E. coli*†

George D. Metcalfe, [a] Thomas W. Smith [a,b] and Michael Hippler *[a]

Nitrate and nitrite reduction to ammonia and nitrous oxide by anaerobic *E. coli* batch cultures is investigated by advanced spectroscopic analytical techniques with ^{15}N-isotopic labelling. Non-invasive, *in situ* analysis of the headspace is achieved using White cell FTIR and cavity-enhanced Raman (CERS) spectroscopies alongside liquid-phase Raman spectroscopy. For gas-phase analysis, White cell FTIR measures CO_2, ethanol and N_2O while CERS allows H_2, N_2 and O_2 monitoring. The 6 m pathlength White cell affords trace gas detection of N_2O with a noise equivalent detection limit of 60 nbar or 60 ppbv in 1 atm. Quantitative analysis is discussed for all four $^{14}N/^{15}N$-isotopomers of N_2O. Monobasic and dibasic phosphates, acetate, formate, glucose and NO_3^- concentrations are obtained by liquid-phase Raman spectroscopy, with a noise equivalent detection limit of 0.6 mM for NO_3^- at 300 s integration time. Concentrations of the phosphate anions are used to calculate the pH *in situ* using a modified Henderson–Hasselbalch equation. NO_2^- concentrations are determined by sampling for colorimetric analysis and NH_4^+ by basifying samples to release $^{14}N/^{15}N$-isotopomers of NH_3 for measurement in a second FTIR White cell. The reductions of $^{15}NO_3^-$, $^{15}NO_2^-$, and mixed $^{15}NO_3^-$ and $^{14}NO_2^-$ by anaerobic *E. coli* batch cultures are discussed. In a major pathway, NO_3^- is reduced to NH_4^+ *via* NO_2^-, with the bulk of NO_2^- reduction occurring after NO_3^- depletion. Using isotopically labelled $^{15}NO_3^-$, $^{15}NH_4^+$ production is distinguished from background $^{14}NH_4^+$ in the growth medium. In a minor pathway, NO_2^- is reduced to N_2O *via* the toxic radical NO. With excellent detection sensitivities, N_2O serves as a monitor for trace NO_2^- reduction, even when cells are predominantly reducing NO_3^-. The analysis of N_2O isotopomers reveals that for cultures supplemented with mixed $^{15}NO_3^-$ and $^{14}NO_2^-$ enzymatic activity to reduce $^{14}NO_2^-$ occurs immediately, even before $^{15}NO_3^-$ reduction begins. Optical density and pH measurements are discussed in the context of acetate, formate and CO_2 production. H_2 production is repressed by NO_3^-; but in experiments with NO_2^- supplementation only, CERS detects H_2 produced by formate disproportionation after NO_2^- depletion.

Received 14th July 2021,
Accepted 15th October 2021

DOI: 10.1039/d1an01261d

rsc.li/analyst

1. Introduction

In the absence of oxygen (O_2), *Escherichia coli* (*E. coli*) can utilise alternative terminal electron acceptors for anaerobic growth, such as nitrate (NO_3^-) and nitrite (NO_2^-). The sequence of reductions from NO_3^- to NO_2^- to ammonia (NH_3, NH_4^+ at physiological pH) is generally referred to as Dissimilatory Nitrate Reduction to Ammonia (DNRA).[1] The coupling of these reductions to the oxidation of organic substrates, such as formate, enables the generation of a proton gradient across the cytoplasmic membrane. DNRA is considerably more efficient for obtaining energy than the mixed acid fermentation pathways utilised when electron acceptors are unavailable. The expression of the respiratory NO_3^- and NO_2^- reductases is tightly controlled by FNR, an O_2 sensitive transcription factor, and NarXL/NarQP, both of which are two-component NO_3^-/NO_2^- sensitive regulatory systems.[2,3]

Although DNRA is the major NO_3^- reduction pathway in *E. coli*, the bacterium also generates minor amounts of the toxic radical nitric oxide (NO) from NO_2^- reduction. The low

[a]*Department of Chemistry, University of Sheffield, Sheffield S3 7HF, UK. E-mail: M.Hippler@sheffield.ac.uk*
[b]*School of Chemical Engineering and Analytical Science, University of Manchester, Manchester M13 9PL, UK*

†Electronic supplementary information (ESI) available: S.1. Key nitrate and nitrite reduction enzymes, S.2. M9 medium formulation, S.3. FTIR spectroscopy of CO_2 and ethanol, S.4. cavity enhanced Raman spectroscopy (Experimental details, spectral fitting procedures and calibration plots), S.5. liquid phase Raman spectroscopy (Experimental details of the home-built Raman spectrometer, spectral fitting procedures and calibration plots) and S.6. analysis of bacterial culture samples (nitrite colorimetry, $^{14}N/^{15}N$-ammonium analysis). See DOI: 10.1039/d1an01261d

level of NO production by *E. coli* may be due to disproportionation of NO_2^- under acidic conditions or non-specific reduction by metalloproteins. The NADH-dependent cytoplasmic NO_2^- reductase (NirB),[4] the membrane-bound periplasmic NO_2^- reductase (NrfA)[5] and the major anaerobic NO_3^- reductase (NRA)[6,7] have all been proposed to be significant sources of NO formation as a by-product of their roles in the DNRA pathway. Aerobically, flavohemoglobin (Hmp) detoxifies NO by oxidation back to NO_3^-; while anaerobically, NO is reduced further to nitrous oxide (N_2O) reportedly by Hmp,[8] flavorubredoxin (NorV)[9] and hybrid cluster protein (Hcp).[10] N_2O is comparatively less toxic than NO and can rapidly diffuse out of the cell. *E. coli* is not a true denitrifier but N_2O production by NO_3^- respiring *E. coli* cultures does share similarities with the denitrification pathway of NO_3^- to nitrogen (N_2) *via* NO_2^-, NO and N_2O. A summary of DNRA and NO generation and detoxification is shown in Fig. 1.

As a model organism, DNRA has been studied extensively in *E. coli*; however, comparatively less is known about the minor pathway leading to N_2O and how its generation differs between NO_3^- and NO_2^- respiring cultures. To gain a better mechanistic understanding, monitoring the key compounds and parameters of these processes is essential. Accurate and reliable analytical techniques are crucial for understanding cell biochemistry and pathway elucidation. This represents a challenge for analytical chemistry, requiring a combination of advanced analytical techniques.

Mass spectrometry and chromatographic techniques are widely applicable to the detection and quantification of a broad range of metabolites.[11] The tandem gas chromatography-mass spectrometry technique is considered the gold standard for the general analysis of volatile organic chemicals.[12] Despite this, these techniques are not readily applicable to rapid, online analysis either due to the need for sampling or for downstream chemical/physical processing before analysis can occur. Electrochemical sensors are widely used for monitoring pH, conductivity, dissolved O_2 and various other chemical species,[13] including NO.[14] Often such sensors are susceptible to cross-interferences from other species, changes in solution activity and long-term drift. For microbiological studies, the need for physical contact between the electrode and cell culture increases the risk of contamination, particularly in continuous cultures, and requires that the electrode is stable towards sterilisation.[11]

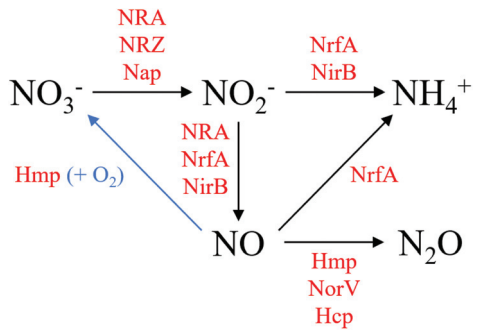

Fig. 1 DNRA and NO generation and detoxification by *E. coli*. Enzymes are displayed in red: **Hcp**, hybrid cluster protein; **Hmp**, flavohemoglobin; **Nap**, periplasmic nitrate reductase, **NirB**, NADH-dependent nitrite reductase; **NorV**, flavorubredoxin; **NRA**, nitrate reductase A; **NrfA**, periplasmic nitrite reductase; **NRZ**, nitrate reductase Z.

Spectroscopic techniques can be readily applied for monitoring bioprocesses *in situ* and online, with no sampling. Vibrational spectroscopic techniques, such as Fourier Transform Infrared (FTIR) and Raman spectroscopies, show high specificity for different molecules due to characteristic spectral bands, making them potentially very valuable for metabolic studies. Additionally, vibrational spectroscopies can distinguish different isotopologues and isotopomers, allowing online monitoring of isotope labelling experiments.[15,16] Good sensitivities are observed in the condensed phase, but measuring headspace gases often suffers from low sensitivity, and special enhancement techniques are required such as Cavity Enhanced Raman Spectroscopy (CERS)[15–22] or long-path absorption White cells in FTIR spectroscopy.[23] Partial pressures in the headspace can be converted into concentrations in the solution *via* Henry's law. Quantum Cascade Laser (QCL) absorption spectroscopy has been applied to detect N_2O and other trace gases;[24–26] while sensitive, the limited tuning range of QCLs over a single IR absorption band limits the dynamic range due to band saturation effects. While FTIR spectroscopy has found some application in bioprocess monitoring, the broad absorption profile of water limits its application for monitoring metabolites at low concentrations in solution. In the gas-phase, the lack of an extended hydrogen network confines the absorption of water to certain spectral regions; molecules with absorption bands outside these regions can be readily detected, even in the presence of high levels of water vapour. Since Raman spectroscopy is comparatively insensitive to water, it is more readily applied to direct monitoring of the liquid-phase. However, fluorescence in complex media such as Lysogeny Broth (LB) can complicate the detection of the comparatively weak Raman light. Fluorescence can be avoided by moving to longer excitation wavelengths or by using media free of fluorescent components, such as M9 minimal media.[23] Vibrational spectroscopic tools have been previously applied to monitoring NO_3^- metabolism in bacteria; CERS has been used to follow N_2O and N_2 production in denitrifying organisms, with the use of $^{15}NO_3^-$ to produce $^{15}N_2$ distinguishable from background $^{14}N_2$.[19,22] A robust CERS instrument has also been designed for field application to study the gas composition of soil samples.[21]

We report a combined approach for characterizing DNRA and N_2O production in anaerobic *E. coli* batch cultures using mostly non-invasive spectroscopic techniques. Sampling of the bacterial culture was only done for NO_2^- colorimetry and FTIR detection of $^{14}NH_3$ and $^{15}NH_3$ isotopomers. Headspace gas analysis was provided by the complementary techniques of FTIR and CERS, with CERS being a technique recently introduced by us in this Journal.[17] FTIR allowed detection of CO_2, ethanol and N_2O while CERS enabled monitoring of the homo-

nuclear diatomic molecules N_2, O_2 and H_2. Recently we introduced the capability of liquid culture analysis by Raman spectroscopy to monitor the microbial fermentation products of acetate and formate and the resulting *in situ* pH from phosphate signatures using a modified Henderson–Hasselbalch equation.[23] Here, we report on improvements that also allowed NO_3^- and glucose analysis during DNRA. With the use of ^{15}N-labelling, we report on mechanistic insights into NO_3^- and NO_2^- reduction to NH_4^+ and N_2O through interpreting the different $^{14}N/^{15}N$-isotopomers produced. The aims of this report are to introduce and characterise a unique combination of advanced spectroscopic techniques with great potential for bioanalytical applications, and to introduce an interesting biochemical application, a ^{15}N-isotope labelling study on N_2O production during DNRA by *E. coli*, with a focus on the differences observed between NO_3^- and NO_2^- reduction.

2. Experimental

Fig. 2 shows a scheme of our experimental setup. Since the previous iteration,[23] it was modified to include CERS for H_2, N_2 and O_2 detection with larger headspace and culture volumes to compensate for more frequent sampling. 250 mL of bacterial batch culture is contained in a round bottom flask with two side-arm ports and submerged in a 37 °C thermostated water bath. From the left side-arm, the bacterial suspension is circulated using a peristaltic pump ($PP_{(l)}$, 4.5 L h^{-1}) for *in situ* OD_{600} (optical density at 600 nm in a 1 cm cuvette) and Raman spectroscopy measurements. From the central-neck, the headspace (1425 mL volume) is cycled by a second peristaltic pump ($PP_{(g)}$, 4.5 L h^{-1}) for gas-phase FTIR and CERS analysis. The right side-arm has a rubber septum enabling sampling of the liquid culture for further analysis. The CERS cavity is equipped with a capacitance pressure gauge (PG), N_2 inlet and vacuum line for purging O_2 to give anaerobic growth conditions (1 atm N_2) before starting experiments.

Production of CO_2, ethanol and N_2O was quantified by gas-phase FTIR spectroscopy (Mattson Research Series, 0.4 cm^{-1} spectral resolution, MCT detector) with a home-built multiple-pass absorption White cell.[23] The White cell pathlength was adjustable between 4–8 m, with 6 m used for this work. Spectra were recorded every 5 minutes. CO_2 partial pressures were obtained by integrating the $\nu_1 + 2\nu_2 + \nu_3$ band (4920–5015 cm^{-1}, ν_0 = 4978 cm^{-1}) of the Fermi triad and comparing with a reference spectrum from the PNNL database.[27] N_2O partial pressures were obtained by integrating the $2\nu_1$ combination band from 2460–2580 cm^{-1} and comparing the integral with simulated spectra from HITRAN 2012.[28] All four $^{14}N/^{15}N$-isotopomers of N_2O could be distinguished, which enabled the ^{15}N-isotope labelling studies. A multiplier equivalent to ethanol partial pressure was obtained by a least-squares fit of 1 ppmv ethanol and water reference spectra in the 2800–3100 cm^{-1} region.[23] Using Henry's law, all partial pressures could be converted into concentrations in solution. Using the ideal gas law, we estimated that 10% of the CO_2 present in the sample was dissolved. Under our conditions, less than 1% of dissolved CO_2 was expected to be converted to carbonic acid and carbonates. 7% of N_2O and 99.7% of ethanol in the sample were also calculated to be dissolved.

The CERS setup has been described before with some modifications outlined below.[15–17,20] A 40 mW 636 nm single-mode cw-diode laser (HL63133DG) is coupled *via* a short-pass filter, a Faraday isolator and a mode matching lens into a linear optical cavity composed of two highly reflective mirrors (Newport SuperMirrors, R > 99.99%). If the laser wavelength

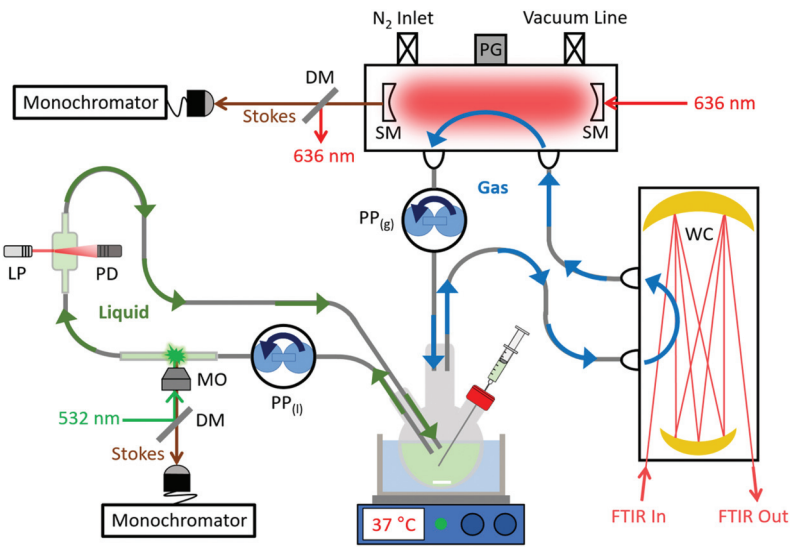

Fig. 2 Experimental setup for analysing the headspace by CERS and White cell FTIR spectroscopies and the liquid culture by Raman spectroscopy and *in situ* OD_{600} measurements. **DM**, dichroic mirror; **LP**, laser pointer; **MO**, microscope objective; **PD**, photodiode; **PG**, pressure gauge; **$PP_{(g)}$**, gas-phase peristaltic pump; **$PP_{(l)}$**, liquid-phase peristaltic pump; **SM**, supermirror; **WC**, White cell.

matches the cavity length, an optical resonance builds up optical power inside the cavity by up to 3 orders of magnitude, enhancing the Raman signals. After the cavity, a dichroic mirror separates leftover excitation light from Raman signals which are coupled into a round-to-linear glass fibre bundle (7 × ∅ 105 μm) and transferred to the monochromator (Andor Shamrock SR163, 1200 l mm^{-1} grating, DV420A-OE CCD). The 400–2500 cm^{-1} spectral range at 6 cm^{-1} resolution encompasses rotational *S*-branch lines of H_2, the $\nu_1/2\nu_2$ Fermi resonance of CO_2 and the vibrational fundamentals of O_2 and N_2. Part of the leftover excitation light is diverted back to the diode for optical feedback, locking the laser to the cavity. To normalize Raman signals, the N_2 peak is used as an internal standard since N_2 is not expected to change during bacterial activity. Raman intensities are converted to partial pressures using tabulated integrated peak areas.[20] CO_2 analysis by CERS was used to corroborate the FTIR analysis; however, CERS CO_2 data was not displayed in this study due to FTIR CO_2 detection being more sensitive. More details of the modified CERS setup are provided in the ESI.†

The bacterial suspension was circulated through a glass cuvette (1 cm path length) and the optical density OD_{600} was recorded *in situ* by measuring the scattering of red laser pointer light with a photodiode. The transmitted intensity was calibrated with start and end-point OD_{600} values externally measured using a UV-Vis spectrometer. The suspension was also circulated through a sealed borosilicate tube for recording liquid-phase Raman spectra using a home-built spectrometer.[29,30] A 532.2 nm, 20 mW laser (Lasos, GL3dT) and monochromator (Shamrock SR-750-A, 1200 l mm^{-1} grating, DU420A-OE CCD) provided a spectral range from 830–1710 cm^{-1} at about 0.8 cm^{-1} resolution. Raman spectra were recorded every 5 minutes at 300 s integration time. No interfering fluorescence was noticeable in M9 minimal growth medium. The water bending vibration at 1630 cm^{-1} was used to normalise decreasing Raman intensities as the turbidity of the bacterial suspension increased.[23] 0.1 M reference spectra of individual glucose, KNO_3, $CH_3CO_2NH_4$, HCO_2K, K_2HPO_4 and KH_2PO_4 solutions were recorded. As shown in Fig. 3, the 830–1200 cm^{-1} region contains characteristic Raman peaks for HPO_4^{2-} (989 cm^{-1}), $H_2PO_4^-$ (876 and 1076 cm^{-1}), NO_3^- (1049 cm^{-1}) and glucose (960–1180 cm^{-1}).[31] Using a least-squares fitting routine, Raman spectra of the bacterial suspension in this region were fitted to the reference spectra, as well as a linear baseline. The returned multipliers of the reference spectra were then converted into concentrations *via* calibration plots. Noise analysis of background sample measurements (pure water) provided noise equivalent (1σ) detection limits of 0.6 mM NO_3^- and 1.9 mM glucose at 300 s integration time. With additional averaging to an integration time of 0.5 h (as was done with all time-dependent data displayed in this study), the limits improve to 0.25 mM for nitrate and 0.8 mM for glucose. The concentrations of the phosphate anions were used to calculate the pH *in situ* using a modified Henderson–Hasselbalch equation.[23,32] A least-squares fit determined acetate and formate concentrations in the 1310–1450 cm^{-1} region to the sum of acetate (1414 cm^{-1}) and formate (1349 cm^{-1}) models and a linear baseline, as shown in the ESI.† At 300 s integration time, the noise equivalent (1σ) detection limits of acetate and formate were 2.6 mM and 1.5 mM, respectively. These limits improve to 1.1 mM and 0.6 mM with additional averaging to 0.5 h integration time. Although NO_2^- has a peak at 1326 cm^{-1}, the feature was too weak to be used in this study (1σ = 5.0 mM). Furthermore, NH_3/NH_4^+ had no usable features within our spectral range.

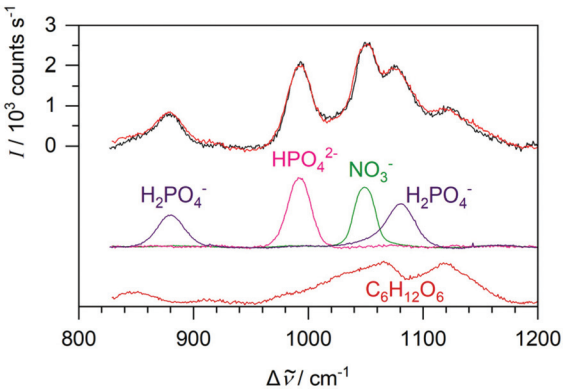

Fig. 3 In black, an experimental Raman spectrum of M9 medium supplemented with 10 mM KNO_3 and 30 mM glucose. In red, the sum of the fitted NO_3^-, glucose, HPO_4^{2-} (47 mM) and $H_2PO_4^-$ (22 mM) models shown below the overlaid spectra.

E. coli (strain K-12 MG1655) was transferred from glycerol stock (maintained at −80 °C) and streaked on LB-agar plates. Plates were left to grow overnight at 37 °C. Before a measurement, 50 mL of sterile LB medium was inoculated with a single colony and incubated anaerobically in a sealed 50 mL centrifuge tube for 16 h (37 °C, 200 rpm) to a typical OD_{600} of 1.2. From the starter culture, 20 mL was centrifuged, and the pellet resuspended into 20 mL of fresh M9 minimal medium. Our M9 medium formulation is given in the ESI;† but notably, it contains 30 mM glucose and 18 mM NH_4Cl. The M9 medium was supplemented with 10 mM $K^{15}NO_3$ (10 mM, 98 atom % ^{15}N, Sigma-Aldrich) and/or 5 mM KNO_2 (either ^{14}N or ^{15}N). A further 230 mL of M9 medium was prepared in the round bottom flask with two side-arms. The flask was pre-warmed and maintained at 37 °C using a thermostated water bath under rapid stirring to enable efficient gas transfer. The 20 mL M9 medium containing *E. coli* was added to the 230 mL M9 medium in the flask, giving a typical starting OD_{600} of 0.1. The flask was then sealed and purged of O_2 by alternating between evacuating the headspace and refilling with N_2 at least five times. Experiments began once CERS measurements confirmed no O_2 remained.

During experiments, 1 mL of the bacterial culture was sampled every 40 min and centrifuged. The supernatant was analysed using a colorimetric method to determine NO_2^- concentration based on the Griess test.[33] Our M9 media began with a typical pH of 6.9 and ended between 5.0–5.5 due to organic acid excretion. With a pK_a of 9.25, NH_3 exists almost

entirely as NH_4^+ at acidic pH. For $^{14}N/^{15}N$-analysis of NH_4^+ samples, 2 mL 1 M NaOH was added to 0.6 mL of sample to release NH_3. The gas was analysed by a second FTIR setup (Bruker Alpha FTIR, 0.8 cm^{-1} spectral resolution) with a home-built White cell (2.0 m pathlength). Spectra were recorded every 5 minutes with around 30 minutes needed before NH_3 concentration peaked in the headspace. The basified solution was rapidly stirred and the 2 L headspace in the closed system was cycled between the sample flask and White cell using a peristaltic pump. The ν_2 band is the strongest in the FTIR spectrum of NH_3 and can be used for $^{14}N/^{15}N$-analysis.[34] At the end of bacterial activity, the suspension was centrifuged, washed and dried to record the dry biomass (typically around 200 mg when corrected for sampling). For comparison with the *in situ* spectroscopic pH measurements, the pH of start and end-point samples was recorded externally using a Mettler Toledo SevenMulti pH meter. See the ESI† for further experimental spectra and calibration plots for all aforementioned analytical techniques.

3. Results and discussion

3.1 FTIR spectroscopy of N_2O and its $^{14}N/^{15}N$-isotopomers

N_2O has four $^{14}N/^{15}N$-isotopomers, *i.e.*, $^{14}N_2O$, the structural isomers $^{14}N^{15}NO$ and $^{15}N^{14}NO$, and $^{15}N_2O$. N_2O is amenable to ^{15}N-isotope labelling studies due to the low natural abundance of the ^{15}N-isotope (0.37%). In the 2000–3000 cm^{-1} spectral range, characteristic partially rotationally resolved bands of the N_2O isotopomers are available for FTIR analysis. Apart from *ca.* 2250–2400 cm^{-1} which is saturated by CO_2, this region is free from significant spectral interferences. The HITRAN molecular database contains line lists for the three most abundant $^{14}N/^{15}N$-isotopomers, excluding $^{15}N_2O$.[28] A survey of HITRAN and our experimental spectra has shown that the following vibrational bands are available for quantitative analysis, including band position of $^{14}N_2O$, integrated absorption cross-sections G and peak absorbances A_{peak} (defined as $\ln(I_0/I)$) under our experimental conditions for 1 μbar (1 ppmv) at 6 m path length: the ν_3 fundamental near 2224 cm^{-1} with $G = 5.55 \times 10^{-17}$ cm and $A_{peak} \approx 0.023$ for rotational lines in the *P*- and *R*-branches, the $2\nu_1$ overtone near 2563 cm^{-1} with $G = 1.33 \times 10^{-18}$ cm and $A_{peak} \approx 6 \times 10^{-4}$ for rotational features in the *P*- and *R*-branches, and the $\nu_2 + \nu_3$ combination near 2798 cm^{-1} with $G = 9.0 \times 10^{-20}$ cm and $A_{peak} \approx 2.6 \times 10^{-4}$ of its *Q*-branch. Characteristic spectral shifts allow distinction of the isotopomers, while their G and A_{peak} values remain essentially the same. For accurate quantitative results, A_{peak} should not exceed unity. The dynamic range of the ν_3 fundamental thus extends from trace levels up to *ca.* 45 μbar N_2O, the $2\nu_1$ overtone up to 1.7 mbar, and the $\nu_2 + \nu_3$ combination up to 3.8 mbar. This range can be extended by reducing the absorption pathlength of the White cell.

Fig. 4 shows the ν_3 fundamental with distinct *P*- and *R*-branch features, with $^{14}N_2O$ having its origin near 2224 cm^{-1}. In a spectrum containing only $^{14}N_2O$, a least-squares fit to the reference spectrum in the region denoted '**D**' in Fig. 4 returns a multiplier which corresponds to N_2O partial pressure. A simple integration over the ν_3 band would not be suitable because part of the *R*-branch is buried in $^{13}CO_2$ absorptions at higher wavenumbers. The region '**D**' was selected because it has some of the strongest absorption features, it is very characteristic with partially resolved lines, and it is least affected by CO_2. With this fitting routine, noise analysis of blank samples provides a noise equivalent detection limit of 60 nbar (60 ppbv at 1 bar total pressure) at 6 m pathlength and 128 accumulations which take 2 min to acquire. Detection limits can be improved by more averaging or increasing the path length. Note that this is sufficient to detect the 330 ppbv ambient levels of N_2O for environmental analytical applications. The heavier isotopomers shift to lower wavenumbers, 2201 cm^{-1} for $^{15}N^{14}NO$, 2178 cm^{-1} for $^{14}N^{15}NO$, and 2155 cm^{-1} for $^{15}N_2O$. Since the bands are overlapping, only a simultaneous fit to all four model spectra can yield individual isotopomer partial pressures. A fit in the entire 2100–2220 cm^{-1} region, however, has serious problems with cross-correlations. After a careful analysis, a simultaneous fit only including the regions '**A**' to '**D**' in Fig. 4 returned multipliers which are not noticeably affected by cross-correlations. Each region was chosen so that an individual isotopomer has a maximum weight with the other isotopomers having as little weight as possible. This procedure yields reliable isotopic partial pressures up to a dynamic range of about 45 μbar per isotopomer.

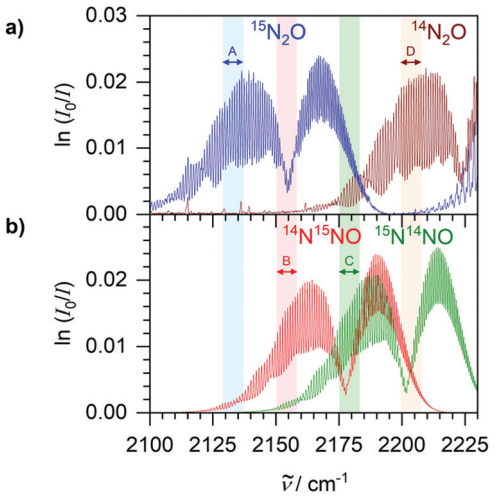

Fig. 4 ν_3 fundamental of N_2O isotopomers with partially resolved rotational *P*- and *R*-branches. Absorbances scaled to correspond to 1 μbar (1 ppmv) at 6 m path length. (a) Experimental FTIR spectra of $^{15}N_2O$ (blue) and $^{14}N_2O$ (brown). (b) Isotopomers (structural isomers) $^{14}N^{15}NO$ (red) and $^{15}N^{14}NO$ (green) calculated from the HITRAN database. A to D denotes spectral ranges used in the fit.

Fig. 5 shows the weaker absorption bands that are more suitable for N_2O analysis above 45 μbar. In isotopically pure samples, the $2\nu_1$ overtone near 2563 cm^{-1} can be integrated from 2505–2613 cm^{-1} to obtain $^{14}N_2O$ partial pressure after

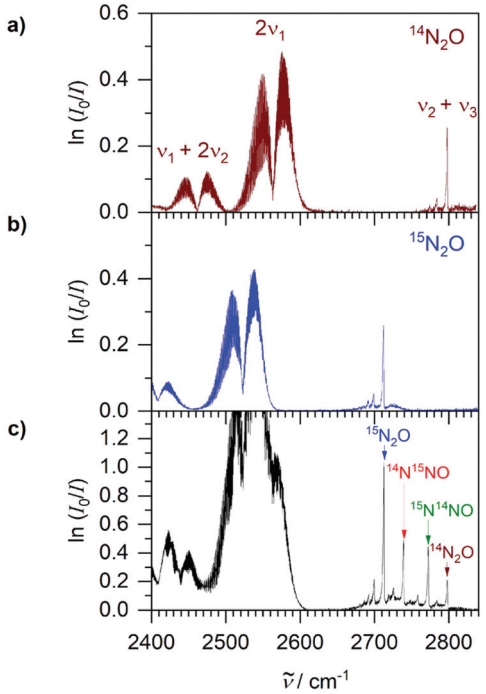

Fig. 5 Experimental FTIR spectra of N_2O overtone and combination bands for (a) 1 mbar $^{14}N_2O$, (b) 1 mbar $^{15}N_2O$ and (c) a mixture of 2.8 mbar $^{15}N_2O$ (49%), 1.1 mbar $^{14}N^{15}NO$ (20%), 1.2 mbar $^{15}N^{14}NO$ (22%) and 0.5 mbar $^{14}N_2O$ (9%). The isotopomer mixture was recorded at 30 h during the anaerobic respiration of *E. coli* supplemented with 10 mM $^{15}NO_3^-$ and 5 mM ^{14}N-nitrite (see section 3.4).

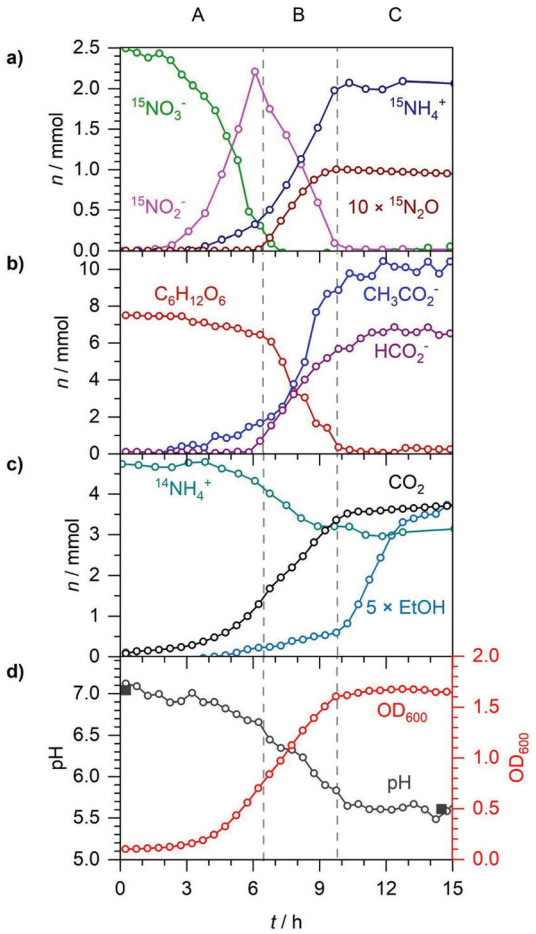

Fig. 6 Anaerobic *E. coli* growth in M9 medium supplemented with 10 mM $^{15}NO_3^-$. **A** to **C** denotes three distinct phases: NO_3^- reduction (A), NO_2^- reduction (B) and NO_2^- depletion (C). (a) Time-dependent number of moles (n) of $^{15}NO_3^-$, $^{15}NO_2^-$, $^{15}NH_4^+$ and $^{15}N_2O$ (x10). (b) n of glucose, acetate and formate. (c) n of CO_2, ethanol (x5) and $^{14}NH_4^+$. (d) Spectroscopically determined pH (open circles), externally measured pH (solid squares) and OD_{600}.

comparison with a reference spectrum (Fig. 5a). For $^{15}N_2O$ the shifted band near 2523 cm^{-1} can be integrated from 2460–2580 cm^{-1} (Fig. 5b). In samples with mixtures of isotopomers (Fig. 5c), the $2\nu_1$ bands overlap and require a more sophisticated simultaneous fit similar to the one described above for the ν_3 fundamental. Fortunately, this is not required as the $\nu_2 + \nu_3$ combination band (2798 cm^{-1} for $^{14}N_2O$) has a sharp, characteristic Q-branch which remains well resolved and separated in isotopic mixtures. After comparison with reference spectra, simple integrations over the separate Q-branch peaks yield isotopic partial pressures in a mixture up to a dynamic range of about 3.8 mbar.

3.2 Spectroscopic analysis of nitrate reduction by *E. coli*

Fig. 6 is a typical example of pH, OD_{600} and number of moles (n) of electron acceptors and other metabolites measured during the reduction of 10 mM $^{15}NO_3^-$ by anaerobic *E. coli*. Concentrations (mM) in solution were converted to n (mmol) by multiplying by the culture volume (0.25 L), as were partial pressures using the ideal gas law ($V = 1.425 \times 10^{-3}$ m^3, T = 310 K) and correcting for the dissolved percentage calculated *via* Henry's law. All biological experiments were repeated in triplicate, and all repeats showed essentially the same behaviour. The time-dependent data displayed in this study is for a single representative experiment selected from the repeats. Phase **A** (0–6.5 h) lasted until all NO_3^- was reduced to NO_2^-. Phase **B** (6.5–10 h) lasted until all NO_2^- was reduced to NH_4^+ and N_2O. Phase **C** (>10 h) had no electron acceptors remaining so the bacteria utilised fermentative pathways solely. The ^{15}N-label transferred to $^{15}NH_4^+$ and $^{15}N_2O$ with no trace of other N_2O isotopomers formed. This was consistent with other studies that found the N-atoms in N_2O both originate from NO_3^-/NO_2^- and not other sources such as N_2 or NH_4^+.[19,22,35] The externally measured start and end-point pH measurements showed good agreement with the time-dependent spectroscopically determined pH.

After a brief lag phase, exponential growth began at 3 h with a rapid increase in the OD_{600}. NO_3^- reduction to NO_2^- mirrored the growth curve with most of the NO_2^- produced excreted to prevent cytoplasmic toxification.[36] *E. coli* expresses three NO_3^- reductases: the respiratory NO_3^- reductases A and Z (NRA and NRZ) and the periplasmic NO_3^- reductase (Nap).[37–39] NRA is the most active reductase at high NO_3^- levels (>2 mM).[40] Nap is induced by low NO_3^- levels, while

NRZ is expressed at low levels constitutively and may function under stress-associated conditions.[40–42] NO_2^- peaked at 2.2 mmol, less than the initial 2.5 mmol NO_3^-, as some NO_2^- was reduced alongside NO_3^- during **A**. 0.3 mmol $^{15}NH_4^+$ and 1.6 μmol $^{15}N_2O$ was produced, accounting for the total N-balance. Only 1% of the 0.3 mmol NO_2^- reduced in **A** was converted to N_2O instead of NH_4^+. *E. coli* expresses two NO_2^- reductases: the NADH-dependent cytoplasmic NO_2^- reductase (NirB) and the membrane-bound periplasmic NO_2^- reductase (NrfA). NirB likely produced NH_4^+ during **A** as it is active when NO_3^- is readily available, unlike NrfA.[43] Evidence also suggests NirB can generate NO.[4] Anaerobically, NO is detoxified by reduction to N_2O, which is comparatively non-toxic and rapidly diffuses out of the cell. Flavorubredoxin (NorV),[9] hybrid cluster protein (Hcp),[10] NirB[44] and NrfA[45] have all been proposed to have NO detoxifying activity. Flavohemoglobin (Hmp) is primarily an NO oxidase but also acts as an NO reductase anaerobically.[8]

As *E. coli* does not possess any known N_2O reductases, further reduction to N_2 was not expected. However, there is some evidence that N_2 can be produced from high amounts of N_2O by a yet unknown mechanism.[46] To investigate whether under our conditions N_2 was produced, we repeated the experiment, but under an argon atmosphere instead of N_2. No trace of N_2 production was observed in the CERS spectra within our detection limit of *ca.* 0.2 mbar or 12 μmol N_2.

Formate oxidation to CO_2 by the NO_3^--inducible formate dehydrogenase (FdhN) is a physiological source of electrons for NO_3^- reduction.[38] Other sources include NADH, lactate and glycerol.[37] 1.7 of the 2.5 mmol NO_3^- reduced was coupled to FdhN activity as CO_2 increased by such in **A**. The remaining 0.8 mmol NO_3^- was likely coupled to NADH oxidation.[47] As no formate was excreted in **A**, all formate produced by pyruvate formate lyase (PFL) must have been oxidised to CO_2. For each formate produced by PFL, one acetyl-CoA is formed which can be either directed into the anaerobic TCA cycle or converted to acetate (to produce ATP) or ethanol (to remove reducing equivalents). 1.7 mmol acetate and 0.05 mmol ethanol were excreted during **A** corresponding to 1.75 mmol formate, in good agreement with the 1.7 mmol CO_2 produced. Acetate must be excreted to prevent cytoplasmic acidification and caused the extracellular pH to decrease from 7.1 to 6.7. The minor amount of ethanol produced was due to reducing equivalents being coupled directly into reduction of NO_3^-. Previous studies have found a similar repression of substrate-level NADH consuming pathways when electron acceptors are available.[48] Glucose decreased by 1.1 mmol owing to the production of CO_2, acetate, ethanol and biomass synthesis.

During phase **B**, NO_2^- was reimported into *E. coli* and reduced. From 6.5 to 10 h, 2.2 mmol $^{15}NO_2^-$ was reduced almost linearly to 2.0 mmol $^{15}NH_4^+$ and 0.1 mmol $^{15}N_2O$. 91% NO_2^- was reduced to NH_4^+ and 9% to N_2O, a higher partitioning to N_2O than observed in **A** (1%). A higher partitioning to N_2O after NO_3^- was depleted is consistent with several studies of *E. coli* and *Salmonella enterica* that have implicated NRA as the enzyme that produces the majority of NO when NO_2^- is abundant and NO_3^- absent.[6,7,49,50] NrfA, which is induced by NO_2^- but repressed by NO_3^-, may have also contributed towards the higher partitioning to N_2O in **B** as it has been proposed as a source of NO.[5,51] The radical NO has a distinct line-resolved absorption band centred at 1904 cm^{-1} (for ^{14}NO) and a favourable partitioning into the headspace.[52] However, no intermediate ^{15}NO gas was observed to accumulate, owing to its rapid detoxification to $^{15}N_2O$ by *E. coli*. During **B**, a further 1.9 mmol CO_2 was produced and the pH dropped from 6.7 to 5.7 due to the excretion of 5.7 mmol formate and a further 7.5 mmol acetate. Due to the 3 : 1 stoichiometry of formate oxidation to $CO_2 : NO_2^-$ reduction to NH_4^+, 0.6 mmol NO_2^- was coupled to formate by NrfA.[53] The 5.7 mmol formate excreted during **B** would be plentiful to couple to the remaining 1.4 mmol NO_2^-. However, NrfA is most active at low NO_2^- levels while NirB is most active at high NO_2^- levels for detoxification of excess NO_2^-.[36,43] Thus, 1.4 mmol NO_2^- was likely reduced by NirB.

Phase **C** started with exponential growth ending as the OD_{600} peaked at 1.7, due to the depletion of glucose and NO_2^-. With no electron acceptors available, the bacteria funnelled reducing equivalents into ethanol as a further 0.7 mmol was made over the next 5 h. The remaining 5.7 mmol formate was slowly oxidised to CO_2 at a rate of 0.03 mmol h^{-1}. Under anaerobic conditions, the presence of formate induces formate hydrogenlyase (FHL) activity that disproportionates formate to CO_2 and H_2.[54] O_2 and NO_3^- repress FHL expression and instead induce the aerobic and the formate-NO_3^- respiratory chains. High formate concentrations can partially reverse the repression by NO_3^-, but not by O_2.[55,56] However, CERS measurements detected no H_2 production during our 10 mM $^{15}NO_3^-$ reduction experiments. During **C**, there was a slight decline in N_2O observed due to the gas adsorbing to tubing and glass surfaces.

Experiments were terminated after 2 days with 5 mmol formate still remaining. The dry biomass was typically around 200 mg. As *E. coli* can be approximated to be 48% carbon and 14% nitrogen by mass,[57] *ca.* 8 mmol C and 2 mmol N in the biomass originated from the 7.5 mmol glucose (45 mmol C) and NH_4^+, respectively. 44 out of the 45 mmol C from glucose can be accounted for in the biomass, 5 mmol CO_2, 5 mmol formate, 12 mmol acetate (24 mmol C) and 1 mmol ethanol (2 mmol C). During exponential growth, $^{14}NH_4^+$ decreased from 4.5 to 3.0 mmol accounting for 1.5 out of the 2 mmol N in the biomass. The remaining 0.5 mmol N likely was taken from the excreted $^{15}NH_4^+$. The 2.5 mmol ^{15}N-label can be accounted for in the 2.0 mmol $^{15}NH_4^+$, 0.1 mmol $^{15}N_2O$ (0.2 mmol ^{15}N) and ~0.5 mmol $^{15}NH_4^+$ used for biosynthesis.

3.3 Spectroscopic analysis of nitrite reduction by *E. coli*

To study the response to NO_2^- alone, anaerobic *E. coli* was supplemented with 5 mM $^{15}NO_2^-$, as shown in Fig. 7. Phase **A′** (0–9 h) corresponded to the reduction of NO_2^- to NH_4^+ with concurrent N_2O production *via* NO. Phase **B′** (9–15 h) was when the bacteria utilised fermentative pathways only, due to NO_2^- depletion. During the first 9 h of phase **A′**, 1.25 mmol

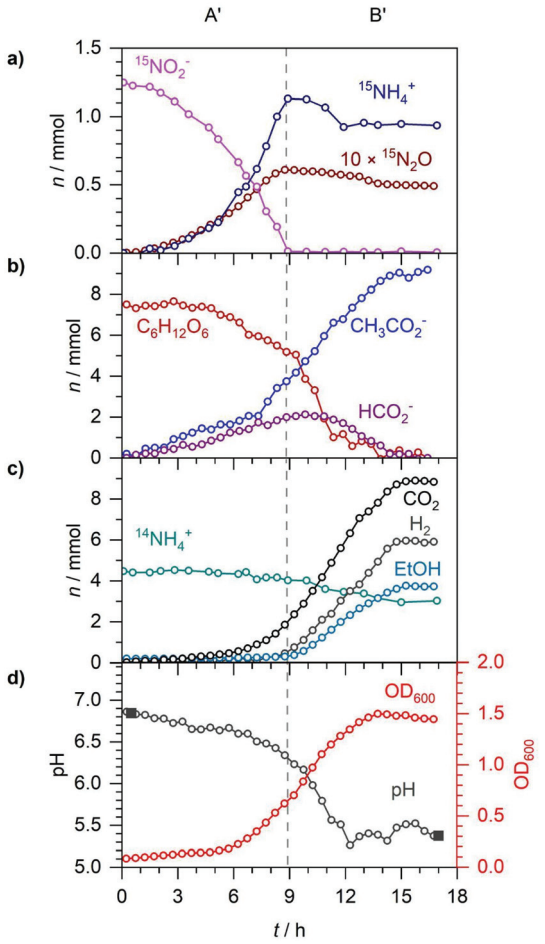

Fig. 7 Anaerobic *E. coli* growth in M9 medium supplemented with 5 mM $^{15}NO_2^-$. **A′** and **B′** denote two distinct phases: NO_2^- reduction (**A′**) and NO_2^- depletion (**B′**). (a) Time-dependent number of moles (*n*) of $^{15}NO_2^-$, $^{15}NH_4^+$ and $^{15}N_2O$ (×10). (b) *n* of glucose, acetate and formate. (c) *n* of CO_2, H_2, ethanol and $^{14}NH_4^+$. (d) Spectroscopically determined pH (open circles), externally measured pH (solid squares) and OD_{600}.

$^{15}NO_2^-$ was reduced almost exponentially to 1.15 mmol $^{15}NH_4^+$ (90%) and 0.06 mmol $^{15}N_2O$ (10%), mirroring the bacterial growth curve which increased to an OD_{600} of 0.7. The 10% partitioning to N_2O here was consistent with the 9% observed during the NO_2^- reduction phase **B** in section 3.2. During **A′**, 1.9 mmol CO_2, 3.7 mmol acetate, 2.0 mmol formate and 0.3 mmol ethanol were produced as glucose decreased from 7.5 to 5.2 mmol. Excretion of acetate and formate caused the pH to decrease from 6.9 to 6.3. The sum of acetate and ethanol (4.0 mmol) showed good agreement with the sum of CO_2 and formate (3.9 mmol). Due to the 3 : 1 stoichiometry of formate oxidation : NO_2^- reduction and 1.9 mmol CO_2 being produced, 0.63 out of the initial 1.15 mmol NO_2^- reduced to NH_4^+ was coupled to formate oxidation to CO_2. The remaining 0.52 mmol NO_2^- was likely reduced *via* coupling to NADH oxidation by NirB.

Phase **B′** began at 9 h when $^{15}NO_2^-$ was depleted. *E. coli* could only utilise fermentative pathways in the absence of NO_2^-. The most notable difference between 10 mM $^{15}NO_3^-$ reduction (discussed in section 3.2), and 5 mM $^{15}NO_3^-$ reduction was H_2 production that occurred after NO_2^- depletion in Fig. 7. No H_2 production was observed during **A′** as formate-dependent NO_2^- reduction likely made the intracellular formate unavailable for FHL induction. The presence of formate is required for FHL expression but it can be made unavailable by coupling to the reduction of electron acceptors. This inhibiting effect has been observed for NO_3^- and trimethylamine *N*-oxide respiring *E. coli* cultures and in both cases the effect could be partially relieved by adding exogenous formate.[56,58] When NO_2^- was depleted, 5.2 mmol glucose remained meaning further formate could be produced during **B′** which may have triggered the induction of FHL. From 9–15 h, 6.0 mmol H_2 and a further 6.0 mmol CO_2 were produced from the disproportionation of formate. At 10 h, there was a peak of 2.1 mmol formate excreted. During **B′**, a further 5.3 mmol acetate and 3.5 mmol ethanol were produced. By 12 h, the pH dropped to 5.4 and then remained stable as 1.6 mmol acetate was produced and balanced by the reimport and disproportionation of 1.5 mmol formate. By 14 h, the OD_{600} peaked at 1.5, just before the end of bacterial activity at 15 h due to the depletion of glucose and formate. 42.8 out of the 45 mmol C from glucose can be accounted for in the biomass (~8 mmol C), 8.9 mmol CO_2, 9 mmol acetate (18 mmol C) and 3.8 mmol ethanol (7.6 mmol C). During exponential growth, $^{14}NH_4^+$ decreased from 4.5 to 2.9 mmol as did $^{15}NH_4^+$ from a peak value of 1.15 to 0.9 mmol accounting for 1.85 mmol out of the ~2 mmol N in the biomass.

3.4 Simultaneous nitrate and nitrite reduction

In section 3.2, when *E. coli* was supplemented with NO_3^-, there was a distinct hierarchy of metabolic pathways between phases **A**, **B** and **C**. NO_3^- reduction dominated in **A**, followed by NO_2^- reimport and reduction in **B** and finally fermentation in **C**. However, in **A** it was observed that some NO_2^- was simultaneously reduced alongside NO_3^- to NH_4^+ and N_2O. To further investigate the overlap between the reductions of NO_3^- and NO_2^- in **A**, anaerobic *E. coli* was supplemented with 10 mM $^{15}NO_3^-$ and 5 mM $^{14}NO_2^-$ as shown in Fig. 8 and 9. Phase **A** (0–9 h) lasted until all $^{15}NO_3^-$ was reduced to $^{15}NO_2^-$. Phase **B** (9–30 h) corresponded to the reduction of NO_2^- to NH_4^+ with concurrent N_2O production *via* NO. At 15.5 h, the OD_{600} peaked and exponential growth of *E. coli* ended; thus, phase **B1** (9–15.5 h) was NO_2^- reduction with glucose still present and phase **B2** (15.5–30 h) was NO_2^- reduction during glucose depletion. Fig. 8 displays *n* of $^{15}NO_3^-$, NO_2^-, $^{14}NH_4^+$, $^{15}NH_4^+$ (×10) and N_2O isotopomers in **A**. The complete characterization of bacterial growth is given in Fig. 9.

In phase **A**, 2.5 mmol $^{15}NO_3^-$ was reduced and *ca.* 2.25 mmol $^{15}NO_2^-$ was excreted. NO_2^- colorimetry cannot distinguish between $^{14}NO_2^-$ and $^{15}NO_2^-$, so NO_2^- was observed to increase from 1.25 to 3.5 mmol. During **A**, as in section 3.2, some NO_2^- was reduced alongside $^{15}NO_3^-$ to 0.2 mmol $^{15}NH_4^+$ and N_2O isotopomers. $^{14}NO_2^-$ reduction to $^{14}N_2O$ occurred immediately, with 2.2 μmol $^{14}N_2O$ produced almost linearly by

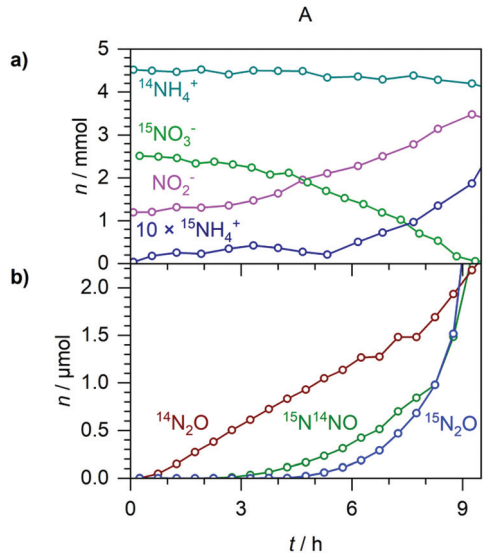

Fig. 8 N_2O isotopomers produced in the NO_3^- reduction phase (**A**) of anaerobic *E. coli* growth in M9 medium supplemented with 10 mM $^{15}NO_3^-$ and 5 mM $^{14}NO_2^-$. (a) Time-dependent number of moles (*n*) of $^{15}NO_3^-$, NO_2^-, $^{14}NH_4^+$ and $^{15}NH_4^+$ (×10). (b) *n* of N_2O isotopomers produced. $^{14}N^{15}NO$ is omitted due to essentially having the same behaviour as $^{15}N^{14}NO$.

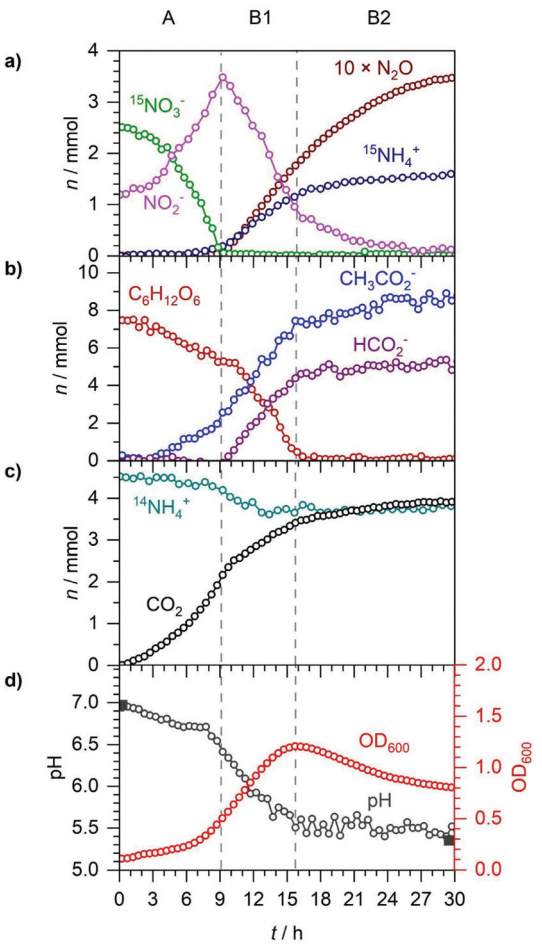

Fig. 9 Anaerobic *E. coli* growth in M9 medium supplemented with 10 mM $^{15}NO_3^-$ and 5 mM $^{14}NO_2^-$. **A** to **C** denotes three distinct phases: NO_3^- reduction (A), NO_2^- reduction with glucose present (B1) and NO_2^- reduction with glucose depleted (B2). (a) Time-dependent number of moles (*n*) of $^{15}NO_3^-$, NO_2^- (both ^{14}N and ^{15}N), $^{15}NH_4^+$ and sum of all $^{14}N/^{15}N$-isotopomers of N_2O (×10). (b) *n* of glucose, acetate and formate. (c) *n* of CO_2 and $^{14}NH_4^+$. (d) Spectroscopically determined pH (open circles), externally measured pH (solid squares) and OD_{600}.

9 h. This indicated that even before NO_3^- reduction began, some unknown enzymatic activity to reduce small quantities of NO_2^- to N_2O was immediately active. For the first 3 h, $^{15}NO_3^-$ and NO_2^- measurements were virtually constant suggesting a lag in the expression of NRA. This lag was best indicated by the highly sensitive positional isomers $^{14}N^{15}NO$ and $^{15}N^{14}NO$ which were not detected until $^{15}NO_2^-$ was made available by $^{15}NO_3^-$ reduction starting from 3 h. $^{15}N_2O$ production also began at 3 h, but much slower than the production of $^{14}N_2O$ and the positional isomers, due to $^{14}NO_2^-$ initially being more readily available than $^{15}NO_2^-$. By the end of **A**, 1.5 µmol each of $^{14}N^{15}NO$, $^{15}N^{14}NO$ and $^{15}N_2O$ were produced alongside the 2.2 µmol $^{14}N_2O$, totalling 6.7 µmol. It is unknown if $^{14}NO_2^-$ was also immediately reduced to $^{14}NH_4^+$, due to the large background of 4.5 mmol $^{14}NH_4^+$ in the growth medium. It can be assumed *ca.* 0.25 mmol NO_2^- was reduced during **A** based on the NO_2^- colorimetry measurements giving a partitioning of 5% NO_2^- reduced to N_2O, instead of NH_4^+. This was a higher value than the 1% observed during **A** in section 3.2, indicating that the added $^{14}NO_2^-$ led to more NO generation and detoxification to N_2O. During **A**, glucose decreased from 7.5 to 5.6 mmol due to the production of 2.1 mmol CO_2, 2.0 mmol acetate and biomass synthesis. The OD_{600} began increasing indicating exponential bacterial growth while acetate excretion caused the pH to decrease from 7.0 to 6.5. No formate was excreted during **A**, as the *n* of CO_2 and acetate suggested all formate formed was oxidised to CO_2. No ethanol was detected during the entire 30 h experiment, likely due to the abundance of electron acceptors to couple reducing equivalents to.

Phase **B1** began with $^{15}NO_3^-$ depletion and ended at 15.5 h when glucose was depleted, coinciding with the OD_{600} peaking at 1.2. The pH dropped further to 5.6 due to the excretion of 5.0 mmol formate and a further 6.0 mmol acetate. The sum of formate excreted and the further 1.3 mmol CO_2 produced was in good agreement with the amount of acetate excreted.

Phase **B2** lasted until NO_2^- depletion at 30 h. From NO_2^- reduction, 1.6 mmol $^{15}NH_4^+$ and 0.35 mmol N_2O were produced overall. The final composition of N_2O isotopomers was previously introduced in Fig. 5c. As the majority of N_2O production occurred in **B** when the NO_2^- composition was *ca.* 66% $^{15}NO_2^-$ and 33% $^{14}NO_2^-$, a near statistical mixture of N_2O isotopomers was formed of 0.17 mmol $^{15}N_2O$ (49%), 0.08 mmol $^{15}N^{14}NO$ (22%), 0.07 mmol $^{14}N^{15}NO$ (20%) and 0.03 mmol $^{14}N_2O$ (9%). For comparison, a perfect statistical mixture would have produced 44.4% $^{15}N_2O$, 22.2% $^{15}N^{14}NO$, 22.2% $^{14}N^{15}NO$ and 11.1% $^{14}N_2O$. It is unknown whether the

slight preference for $^{15}N^{14}NO$ over $^{14}N^{15}NO$ is significant or due to experimental uncertainty. The partitioning of the 3.5 mmol NO_2^- to N_2O in **B** was 20%, a much higher value than the 10% observed during **A** in section 3.2. This is consistent with previous studies that found that between 5–36% of NO_3^- is converted to N_2O by *E. coli*, depending on growth conditions.[35] During **B2**, CO_2 increased by a further 0.5 mmol while the pH remained constant at 5.6 due to no significant change in acetate and formate. 33 out of the 45 mmol C from glucose can be accounted for in the biomass (~8 mmol C), 4 mmol CO_2, 8 mmol acetate (16 mmol C) and 5 mmol formate. The higher NO_2^- content may have had cytotoxic effects in *E. coli* resulting in other products that have not been accounted for in the C balance. During **B2**, the OD_{600} dropped from 1.2 to 0.8 suggesting cell death or changes in cellular size and morphology, possibly due to the cytotoxicity of NO_2^- and NO. The 2.5 mmol ^{15}N label was accounted for in the 1.6 mmol $^{15}NH_4^+$, 0.17 mmol $^{15}N_2O$ (0.34 mmol ^{15}N), 0.08 mmol $^{15}N^{14}NO$, 0.07 mmol $^{14}N^{15}NO$ and *ca.* 0.5 mmol $^{15}NH_4^+$ assumed to have been used for biosynthesis. As *ca.* 2.0 mmol NH_4^+ was needed for biosynthesis, it was assumed *ca.* 1.5 mmol was taken from $^{14}NH_4^+$, which decreased overall from 4.5 to 4.0 mmol suggesting *ca.* 1.0 mmol $^{14}NH_4^+$ produced from the reduction of the 1.25 mmol $^{14}NO_2^-$. This was in good agreement with the 0.26 mmol $^{14}NO_2^-$ reduced to N_2O isotopomers with 0.03 mmol $^{14}N_2O$ (0.06 mmol ^{15}N), 0.08 mmol $^{15}N^{14}NO$ and 0.07 mmol $^{14}N^{15}NO$.

4. Conclusions

We have studied NO_3^- and NO_2^- reduction during DNRA by anaerobic *E. coli* batch cultures by a combination of advanced spectroscopic analytical techniques in conjunction with ^{15}N-isotopic labelling. The online spectroscopic techniques described here are non-invasive, avoiding any contact with the bacterial suspension, and provide concentrations in real-time. We discussed in detail the spectroscopy, which spectral features are most useful for analysis, and data analysis and fitting routines for quantitative analysis. *In situ* analysis of the headspace is achieved using cavity-enhanced Raman (CERS) and long-path White cell FTIR spectroscopies alongside liquid-phase Raman spectroscopy. Gas phase CERS allows CO_2, H_2, N_2 and O_2 monitoring while White cell FTIR measures CO_2, ethanol and N_2O. The 6 m pathlength White cell affords trace gas detection of N_2O with a noise equivalent detection limit of 60 nbar or 60 ppbv in 1 atm (1σ noise equivalent, 128 scans corresponding to 120 s acquisition). This extremely high sensitivity could be utilised in situations where N_2O cannot be allowed to build up, *e.g.* in continuous culture studies. Quantitative analysis is discussed for all four $^{14}N/^{15}N$-isotopomers, including the positional isomers $^{14}N^{15}NO$ and $^{15}N^{14}NO$, a unique capability not available to other analytical techniques.

^{15}N-isotopic labelling of NO_3^- identifies the sources of N-atoms in products of *E. coli* metabolism, in particular, it provides insight into the mechanism of N_2O production during mixed NO_3^- and NO_2^- reduction. This study is one of very few reporting quantitative analysis of N_2O production by *E. coli* under various conditions. The reductions of $^{15}NO_3^-$, $^{15}NO_2^-$, and mixed $^{15}NO_3^-$ and $^{14}NO_2^-$ to NH_4^+ and N_2O have been discussed. In a major pathway, NO_3^- is reduced to NH_4^+ *via* NO_2^-, with the bulk of NO_2^- reduction occurring after NO_3^- depletion. By isotopically labelling $^{15}NO_3^-$, $^{15}NH_4^+$ production is distinguished from background $^{14}NH_4^+$ in the growth medium. In a minor pathway, NO_2^- is reduced to N_2O *via* the toxic radical NO. With excellent detection sensitivities, N_2O monitors trace NO_2^- reduction even when cells are predominantly reducing NO_3^-; the analysis of N_2O isotopomers reveals that some enzymatic NO_2^- reduction activity occurs immediately for cultures supplemented with mixed $^{15}NO_3^-$ and $^{14}NO_2^-$. Optical density and pH measurements are discussed in context of acetate, formate and CO_2 production. H_2 production is repressed by NO_3^-, but with NO_2^- only, CERS detects H_2 produced by formate hydrogenlyase after NO_2^- depletion.

In future work, we want to extend our spectroscopic approach to monitor different bacterial pathways, in particular, the relationship between fermentative and other respiratory pathways and to study nitrifying and denitrifying bacteria. These spectroscopic techniques are capable of detecting key species in the nitrogen cycle and with the ability to sensitively distinguish N_2O isotopomers they may be of great interest for helping better understand global N_2O budgets. Spectroscopic monitoring of bioprocesses has excellent potential to supplement or replace traditional techniques in analytical chemistry.

Author contributions

All authors have contributed equally to the conception of the project, the experimental work, the analysis and to the writing of the manuscript.

Conflicts of interest

The authors declare that they have no conflict of interest.

Acknowledgements

We are grateful to Dr Jim Reid and Profs Jeff Green and Robert Poole for help and discussions. We acknowledge the University of Sheffield and the EPSRC research council (DTP scholarship to GDM) for financial support of our research.

References

1 M. Tiso and A. N. Schechter, Nitrate reduction to nitrite, nitric oxide and ammonia by gut bacteria under physiologi-

cal conditions, *PLoS One*, 2015, **10**, e0127490, DOI: 10.1371/journal.pone.0119712.

2 V. Stewart, Nitrate- and nitrite-responsive sensors NarX and NarQ of proteobacteria, *Biochem. Soc. Trans.*, 2003, **31**, 1–10, DOI: 10.1042/bst0310001.

3 J. Green, M. D. Rolfe and L. J. Smith, Transcriptional regulation of bacterial virulence gene expression by molecular oxygen and nitric oxide, *Virulence*, 2014, **5**, 794–809, DOI: 10.4161/viru.27794.

4 C. E. Vine and J. A. Cole, Nitrosative stress in *Escherichia coli*: reduction of nitric oxide, *Biochem. Soc. Trans.*, 2011, **39**, 213–215, DOI: 10.1042/BST0390213.

5 H. Corker and R. K. Poole, Nitric Oxide Formation by Escherichia coli: Dependence On Nitrite Reductase, The NO-Sensing Regulator Fnr, and Flavohemoglobin Hmp, *J. Biol. Chem.*, 2003, **278**, 31584–31592, DOI: 10.1074/jbc.M303282200.

6 M. S. Smith, Nitrous oxide production by *Escherichia coli* is correlated with nitrate reductase activity, *Appl. Environ. Microbiol.*, 1983, **45**, 1545–1547, DOI: 10.1128/AEM.45.5.1545-1547.1983.

7 R. Metheringham and J. A. Cole, A reassessment of the genetic determinants, the effect of growth conditions and the availability of an electron donor on the nitrosating activity of *Escherichia coli* K-12, *Microbiol.*, 1997, **143**, 2647–2656, DOI: 10.1099/00221287-143-8-2647.

8 S. O. Kim, Y. Orii, D. Lloyd, M. N. Hughes and R. K. Poole, Anoxic function for the *Escherichia coli* flavohaemoglobin (Hmp): reversible binding of nitric oxide and reduction to nitrous oxide, *FEBS Lett.*, 1999, **445**, 389–394, DOI: 10.1016/S0014-5793(99)00157-X.

9 A. M. Gardner, R. A. Helmick and P. R. Gardner, Flavorubredoxin, an Inducible Catalyst for Nitric Oxide Reduction and Detoxification in *Escherichia coli*, *J. Biol. Chem.*, 2002, **277**, 8172–8177, DOI: 10.1074/jbc.M110471200.

10 J. Wang, C. E. Vine, B. K. Balasiny, J. Rizk, C. L. Bradley, M. Tinajero-Trejo, R. K. Poole, L. L. Bergaust, L. R. Bakken and J. A. Coole, The role of the hybrid cluster protein, Hcp and its reductase, Hcr, in high affinity nitric oxide reduction that protects anaerobic cultures of *Escherichia coli* against nitrosative stress, *Mol. Microbiol.*, 2016, **100**, 877–892, DOI: 10.1111/mmi.13356.

11 N. M. Dixon and D. B. Kell, The control and measurement of 'CO_2' during fermentations, *J. Microbiol. Methods*, 1989, **10**, 155–179, DOI: 10.1016/0167-7012(89)90048-1.

12 X. Chen, R. Hu, L. Hu, Y. Huang, W. Shi, Q. Wei and Z. Li, Portable Analytical Techniques for Monitoring Volatile Organic Chemicals in Biomanufacturing Processes: Recent Advances and Limitations, *Front. Chem.*, 2020, **8**, 837, DOI: 10.3389/fchem.2020.00837.

13 S. Sachse, A. Bockisch, U. Enseleit, F. Gerlach, K. Ahlborn, T. Kuhnke, U. Rother, E. Kielhorn, P. Neubauer, S. Junne and W. Vonau, On the use of electrochemical multi-sensors in biologically charged media, *J. Sens. Sens. Syst.*, 2015, **4**, 295–303, DOI: 10.5194/jsss-4-295-2015.

14 M. D. Brown and M. H. Schoenfisch, Electrochemical Nitric Oxide Sensors: Principles of Design and Characterization, *Chem. Rev.*, 2019, **119**, 11551–11575, DOI: 10.1021/acs.chemrev.8b00797.

15 T. W. Smith and M. Hippler, Cavity-Enhanced Raman Spectroscopy in the Biosciences: *In situ*, Multicomponent, and Isotope Selective Gas Measurements To Study Hydrogen Production and Consumption by *Escherichia coli*, *Anal. Chem.*, 2017, **89**, 2147–2154, DOI: 10.1021/acs.analchem.6b04924.

16 G. D. Metcalfe, S. Alahmari, T. W. Smith and M. Hippler, Cavity-Enhanced Raman and Helmholtz Resonator Photoacoustic Spectroscopy to Monitor the Mixed Sugar Metabolism of *E. coli*, *Anal. Chem.*, 2019, **91**, 13096–13104, DOI: 10.1021/acs.analchem.9b03284.

17 R. Salter, J. Chu and M. Hippler, Cavity-enhanced Raman spectroscopy with optical feedback cw diode lasers for gas phase analysis and spectroscopy, *Analyst*, 2012, **137**, 4669–4676, DOI: 10.1039/c2an35722d.

18 R. Keiner, T. Frosch, T. Massad, S. Trumbore and J. Popp, Enhanced Raman multigas sensing - a novel tool for control and analysis of $^{13}CO_2$ labeling experiments in environmental research, *Analyst*, 2014, **139**, 3879–3884, DOI: 10.1039/C3AN01971C.

19 R. Keiner, M. Hermann, K. Küsel, J. Popp and T. Frosch, Rapid monitoring of intermediate states and mass balance of nitrogen during denitrification by means of cavity enhanced Raman multi-gas sensing, *Anal. Chim. Acta*, 2015, **864**, 39–47, DOI: 10.1016/j.aca.2015.02.007.

20 M. Hippler, Cavity-Enhanced Raman Spectroscopy of Natural Gas with Optical Feedback cw-Diode Lasers, *Anal. Chem.*, 2015, **87**, 7803–7809, DOI: 10.1021/acs.analchem.5b01462.

21 A. Sieburg, T. Jochum, S. Trumbore, J. Popp and T. Frosch, Onsite cavity enhanced Raman spectrometry for the investigation of gas exchange processes in the Earth's critical zone, *Analyst*, 2017, **142**, 3360–3369, DOI: 10.1039/C7AN01149K.

22 A. Blohm, S. Kumar, A. Knebl, M. Herrmann, K. Küsel, J. Popp and T. Frosch, Activity and electron donor preference of two denitrifying bacterial strains identified by Raman gas spectroscopy, *Anal. Bioanal. Chem.*, 2021, DOI: 10.1007/s00216-021-03541-y.

23 G. D. Metcalfe, T. W. Smith and M. Hippler, On-line analysis and in situ pH monitoring of mixed acid fermentation by *Escherichia coli* using combined FTIR and Raman techniques, *Anal. Bioanal. Chem.*, 2020, **412**, 7303–7319, DOI: 10.1007/s00216-020-02865-5.

24 J. Mohn, B. Tuzson, A. Manninen, N. Yoshida, S. Toyoda, W. A. Brand and L. Emmenegger, Site selective real-time measurements of atmospheric N_2O isotopomers by laser spectroscopy, *Atmos. Meas. Tech.*, 2012, **5**, 1601–1609, DOI: 10.5194/amt-5-1601-2012.

25 P. Wunderlin, M. F. Lehmann, H. Siegrist, B. Tuzson, A. Joss, L. Emmenegger and J. Mohn, Isotope Signatures of N_2O in a Mixed Microbial Population System: Constraints

of N_2O Producing Pathways in Wastewater Treatment, *Environ. Sci. Technol.*, 2013, **47**, 1339–1348, DOI: 10.1021/es303174x.

26 H. Moser, W. Pölz, J. P. Waclawek, J. Ofner and B. Lendl, Implementation of a quantum cascade laser-based gas sensor prototype for sub-ppmv H_2S measurements in a petrochemical process gas stream, *Anal. Bioanal. Chem.*, 2017, **409**, 729–739, DOI: 10.1007/s00216-016-9923-z.

27 S. W. Sharpe, T. J. Johnson, R. L. Sams, P. M. Chu, G. C. Rhoderick and P. A. Johnson, Gas-Phase Databases for Quantitative Infrared Spectroscopy, *Appl. Spectrosc.*, 2004, **58**, 1452–1461, DOI: 10.1366/0003702042641281.

28 L. S. Rothman, I. E. Gordon, Y. Babikov, A. Barbe, D. Chris Benner, P. F. Bernath, M. Birk, L. Bizzocchi, V. Boudon, L. R. Brown, A. Campargue, K. Chance, E. A. Cohen, L. H. Coudert, V. M. Devi, D. B. Drouin, A. Fayt, J.-M. Flaud, R. R. Gamache, J. J. Harrison, J.-M. Hartmann, C. Hill, J. T. Hodges, D. Jacquemart, A. Jolly, J. Lamouroux, R. J. Le Roy, G. Li, D. A. Long, O. M. Lyulin, C. J. Mackie, S. T. Massie, S. Mikhailenko, H. S. P. Müller, O. V. Naumenko, A. V. Nikitin, J. Orphal, V. Perevalov, A. Perrin, E. R. Polovtseva, C. Richard, M. A. H. Smith, E. Starikova, K. Sung, S. Tashkun, J. Tennyson, G. C. Toon, V. G. Tyuterev and G. Wagner, The HITRAN2012 molecular spectroscopic database, *J. Quant. Spectrosc. Radiat. Transfer*, 2013, **130**, 4–50, DOI: 10.1016/j.jqsrt.2013.07.002.

29 C. Mohr, C. L. Spencer and M. Hippler, Inexpensive Raman Spectrometer for Undergraduate and Graduate Experiments and Research, *J. Chem. Educ.*, 2010, **87**, 326–330, DOI: 10.1021/ed800081t.

30 Y. Ryabenkova, N. Jadav, M. Conte, M. Hippler, N. Reeves-McLaren, P. D. Coates, P. Twigg and A. Paradkar, Mechanisms of Hydrogen-Bonded Complex Formation between Ibuprofen and Nanocrystalline Hydroxyapatite, *Langmuir*, 2017, **33**, 2965–2976, DOI: 10.1021/acs.langmuir.6b04510.

31 M. D. Fontana, K. B. Mabrouk and T. H. Kauffmann, Raman spectroscopic sensors for inorganic salts, in *Spectroscopic Properties of Inorganic and Organometallic Compounds: Techniques, Materials and Applications*, Royal Society of Chemistry, Cambridge, U.K., 2013, vol. 44, pp. 40–67, DOI: 10.1039/9781849737791-00040.

32 M. Hippler and G. D. Metcalfe, Using activities to correct the Henderson-Hasselbalch equation, *Bunsenmagazin*, 2020, **22**, 102–105, DOI: 10.26125/y7p7-an56.

33 M. B. Shinn, Colorimetric Method for Determination of Nitrate, *Ind. Eng. Chem., Anal. Ed.*, 1941, **13**, 33–35, DOI: 10.1021/i560089a010.

34 I. L. Marr, A. Kindness and M. S. Cresser, Measurement of ^{14}N: ^{15}N ratios by Fourier transform infrared spectrometry, *Analyst*, 1987, **112**, 1491–1494, DOI: 10.1039/AN9871201491.

35 B. H. Bleakley and J. M. Tiedje, Nitrous Oxide Production by Organisms Other than Nitrifiers or Denitrifiers, *Appl. Environ. Microbiol.*, 1982, **44**, 1342–1348, DOI: 10.1128/AEM.44.6.1342-1348.1982.

36 T. M. Khlebodarova, N. A. Ree and V. A. Likhoshvai, On the control mechanisms of the nitrite level in *Escherichia coli* cells: the mathematical model, *BMC Microbiol.*, 2016, **16**, S7, DOI: 10.1186/s12866-015-0619-x.

37 V. Stewart, Nitrate respiration in relation to facultative metabolism in enterobacteria, *Microbiol. Rev.*, 1988, **52**, 190–232, DOI: 10.1128/mr.52.2.190-232.1988.

38 V. Bonnefoy and J. A. Demoss, Nitrate reductases in *Escherichia coli*, *Antonie van Leeuwenhoek*, 1994, **66**, 47–56, DOI: 10.1007/BF00871632.

39 V. Stewart, Y. Lu and A. J. Darwin, Periplasmic nitrate reductase (NapABC enzyme) supports anaerobic respiration by *Escherichia coli* K-12, *J. Bacteriol.*, 2002, **184**, 1314–1323, DOI: 10.1128/JB.184.5.1314-1323.2002.

40 H. Wang, C. P. Tseng and R. P. Gunsalus, The *napF* and *narG* Nitrate Reductase Operons in *Escherichia coli* Are Differentially Expressed in Response to Submicromolar Concentrations of Nitrate but Not Nitrite, *J. Bacteriol.*, 1999, **181**, 5303–5308, DOI: 10.1128/JB.181.17.5303-5308.1999.

41 J. Cole, Nitrate reduction to ammonia by enteric bacteria: redundancy, or a strategy for survival during oxygen starvation?, *FEMS Microbiol. Lett.*, 1996, **136**, 1–11, DOI: 10.1016/0378-1097(95)00480-7.

42 L. Chang, L. I. Wei, J. P. Audia, R. A. Morton and H. E. Schellhorn, Expression of the *Escherichia coli* NRZ nitrate reductase is highly growth phase dependent and is controlled by RpoS, the alternative vegetative sigma factor, *Mol. Microbiol.*, 2002, **34**, 756–766, DOI: 10.1046/j.1365-2958.1999.01637.x.

43 H. Wang and R. P. Gunsalus, The *nrfA* and *nirB* Nitrite Reductase Operons in *Escherichia coli* Are Expressed Differently in Response to Nitrate than to Nitrite, *Genet. Mol. Biol.*, 2000, **182**, 5813–5822, DOI: 10.1128/jb.182.20.5813-5822.2000.

44 B. Weiss, Evidence for Mutagenesis by Nitric Oxide during Nitrate Metabolism in *Escherichia coli*, *J. Bacteriol.*, 2006, **188**, 829–833, DOI: 10.1128/JB.188.3.829-833.2006.

45 S. R. Poock, E. R. Leach, J. W. B. Moir, J. A. Cole and D. J. Richardson, Respiratory Detoxification of Nitric Oxide by the Cytochrome *c* Nitrite Reductase of *Escherichia coli*, *J. Biol. Chem.*, 2002, **277**, 23664–23669, DOI: 10.1074/jbc.M200731200.

46 M. Kaldorf, K. H. Linne von Berg, U. Meier, U. Servos and H. Bothe, The reduction of nitrous oxide to dinitrogen by *Escherichia coli*, *Arch. Microbiol.*, 1993, **160**, 432–439, DOI: 10.1007/BF00245303.

47 J. van der Plas, K. J. Hellingwerf, H. G. Seijen, J. R. Guest, J. H. Weiner and W. N. Konings, Identification and localization of enzymes of the fumarate reductase and nitrate respiration systems of *Escherichia coli* by crossed immunoelectrophoresis, *J. Bacteriol.*, 1983, **153**, 1027–1037, DOI: 10.1128/jb.153.2.1027-1037.1983.

48 W. J. Dobrogosz, Altered End-Product Patterns and Catabolite Repression in *Escherichia coli*, *J. Bacteriol.*, 1966, **91**, 2263–2269, DOI: 10.1128/JB.91.6.2263-2269.1966.

49 N. J. Gilberthorpe and R. K. Poole, Nitric oxide homeostasis in *Salmonella typhimurium*, *J. Biol. Chem.*, 2008, **283**, 11146–11154, DOI: 10.1074/jbc.M708019200.

50 C. E. Vine, S. K. Purewal and J. A. Cole, NsrR-dependent method for detecting nitric oxide accumulation in the *Escherichia coli* cytoplasm and enzymes involved in NO production, *FEMS Microbiol. Lett.*, 2011, **325**, 108–114, DOI: 10.1111/j.1574-6968.2011.02385.x.

51 L. Page, L. Griffiths and J. A. Cole, Different physiological roles of two independent pathways for nitrite reduction to ammonia by enteric bacteria, *Arch. Microbiol.*, 1990, **154**, 349–354, DOI: 10.1007/BF00276530.

52 R. H. Gillette and E. H. Eyster, The Fundamental Rotation-Vibration Band of Nitric Oxide, *Phys. Rev.*, 1939, **56**, 1113–1119, DOI: 10.1103/PhysRev.56.1113.

53 A. Abou-Jaoudé, M. Chippaux and M.-C. Pascal, Formate-Nitrite Reduction in *Escherichia coli* K-12. 1. Physiological Study of the System, *Eur. J. Biochem.*, 1979, **95**, 309–314, DOI: 10.1111/j.1432-1033.1979.tb12966.x.

54 J. S. McDowall, B. J. Murphy, M. Haumann, T. Palmer, F. A. Armstrong and F. Sargent, Bacterial formate hydrogenlyase complex, *Proc. Natl. Acad. Sci. U. S. A.*, 2014, **111**, 3948–3956, DOI: 10.1073/pnas.1407927111.

55 A. Pecher, F. Zinoni, C. Jatisatienr, R. Wirth, H. Hennecke and A. Böck, On the redox control of synthesis of anaerobically induced enzymes in enterobacteriaceae, *Arch. Microbiol.*, 1983, **136**, 131–136, DOI: 10.1007/BF00404787.

56 R. Rossmann, G. Sawers and A. Böck, Mechanism of regulation of the formate-hydrogenlyase pathway by oxygen, nitrate and pH: definition of the formate regulon, *Mol. Microbiol.*, 1991, **5**, 2807–2814, DOI: 10.1111/j.1365-2958.1991.tb01989.x.

57 R. Grosz and G. Stephanopoulos, Statistical mechanical estimation of the free energy of formation of *E. coli* biomass for use with macroscopic bioreactor balances, *Biotechnol. Bioeng.*, 1983, **25**, 2149–2163, DOI: 10.1002/bit.260250904.

58 H. Abaibou, G. Giordano and M.-A. Mandrand-Berthelot, Supression of *Escherichia coli* formate hydrogenlyase activity by trimethylamine *N*-oxide is due to drainage of the inducer formate, *Microbiol.*, 1997, **143**, 2657–2664, DOI: 10.1099/00221287-143-8-2657.

Supplementary Material

Advanced Spectroscopic Analysis and ^{15}N-Isotopic Labelling Study of Nitrate and Nitrite Reduction to Ammonia and Nitrous Oxide by *E. coli*

George D. Metcalfe [1], Thomas W. Smith [1,2] and Michael Hippler [1]*

[1] ***Department of Chemistry, University of Sheffield, Sheffield S3 7HF, UK***

[2] ***School of Chemical Engineering and Analytical Science, University of Manchester, Manchester M13 9PL, UK***

[*] ***Corresponding author. E-Mail: M.Hippler@sheffield.ac.uk***

Content:

S.1. Key Nitrate and Nitrite Reduction Enzymes

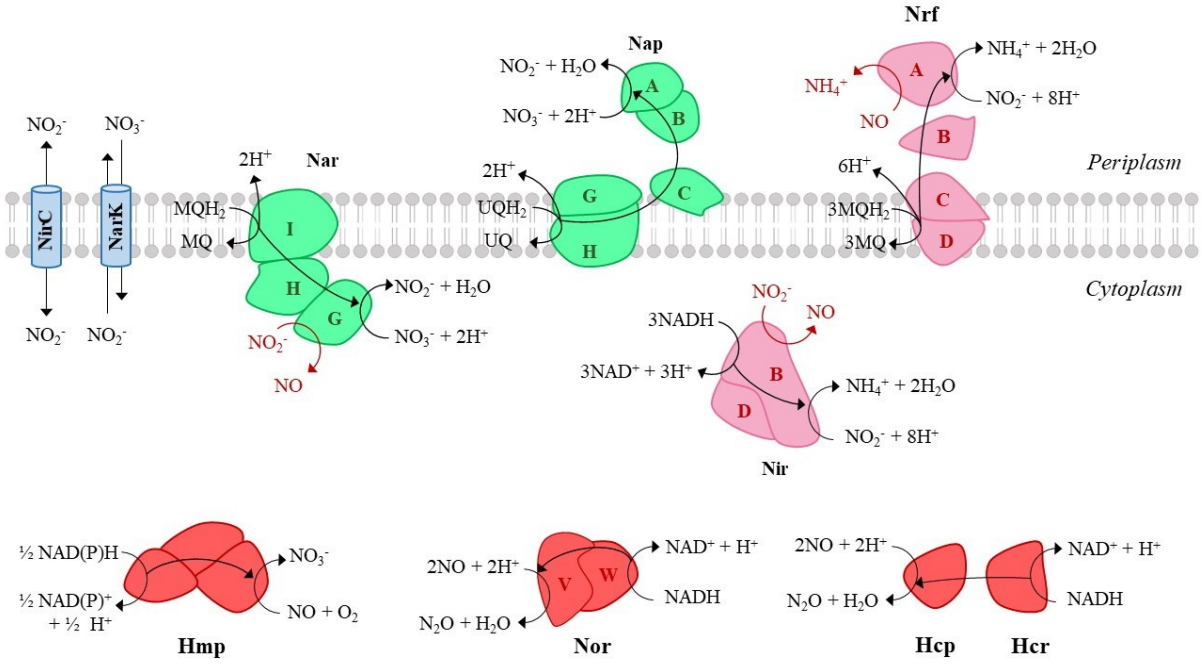

Fig. S1. The cellular locations of key enzymes during NO_3^- and NO_2^- reduction by *E. coli*, including generation or detoxification of NO by NO_3^- and NO_2^- reductases. Enzymes are displayed in boldface: **Hcp**, hybrid cluster protein; **Hcr**, NADH-dependent Hcp reductase; **Hmp**, flavohemoglobin; **NarK**, a NO_3^-/NO_2^- antiporter; **NirB**, NADH dependent NO_2^- reductase; **NirC**, a NO_2^- transporter; **NorV**, flavorubredoxin; **Nap**, periplasmic NO_3^- reductase; **Nar**, NO_3^- reductase A; **NrfA**, periplasmic NO_2^- reductase.

Fig. **S1** shows the cellular locations of key enzymes involved during *E. coli* NO_3^- and NO_2^- reduction. *E. coli* expresses three NO_3^- reductases: the respiratory NO_3^- reductases A and Z (NRA and NRZ) and the periplasmic NO_3^- reductase (Nap) [1–3]. NRA is the major anaerobic NO_3^- reductase active at high NO_3^- levels (> 2 mM) while Nap is induced by low NO_3^- levels [4]. NRZ is expressed at low levels constitutively and may function under stress-associated conditions or in an adaptive role in the transition from aerobiosis to anaerobic NO_3^- respiration [5, 6]. Formate is a physiological source of electrons for NO_3^- reduction that is oxidised to CO_2 by the NO_3^--inducible formate dehydrogenase (FdhN) and transfers electrons to the quinone pool of the membrane [2], other sources include reduced nicotinamide adenine dinucleotide (NADH), lactate and glycerol [1]. NADH-dependent cytoplasmic NO_2^- reductase (NirB) and the membrane-bound periplasmic NO_2^- reductase (NrfA) formally catalyse the six-electron reduction of NO_2^- to NH_3 instead of the one-electron reduction of NO_2^- to NO [7]. Nevertheless, *E. coli* still generates low levels of NO during anaerobic growth on NO_3^-, either from the disproportion of NO_2^- under acidic conditions or non-specific reduction by metalloproteins. NRA (in the absence of NO_3^-) [8–11], NirB [12] and NrfA [13] have all been proposed to be significant sources of NO formation. Both NO_2^- and NO are cytotoxic species and careful control of their intracellular concentration is required, either through detoxification to less reactive species or by excretion. Anaerobically, NO is detoxified by reduction to N_2O, which is comparatively non-toxic and rapidly diffuses out of the cell. Flavorubredoxin (NorV) [14], hybrid cluster protein (Hcp) [15], NirB [16] and NrfA [17] have all been proposed to have NO detoxifying activity. Flavohemoglobin (Hmp) is primarily an NO oxidase but also acts as an NO reductase

anaerobically [18]. As *E. coli* does not possess any known N_2O reductases, further reduction to N_2 is not expected to occur. However, there is some evidence that N_2 might be produced under some conditions by a yet unknown mechanism [19].

S.2. M9 Formulation

Our entire M9 formulation is listed below. To this base formulation we supplemented 10 mM $K^{15}NO_3$ (10 mM, 98 atom % ^{15}N, Sigma Aldrich) and/or 5 mM KNO_2 (either ^{14}N or ^{15}N).

- 48 mM Sodium phosphate dibasic
- 30 mM Glucose
- 22 mM Potassium phosphate monobasic
- 18 mM Ammonium chloride
- 8.5 mM Sodium chloride
- 1 mM Magnesium sulphate
- 1 mM Thiamine hydrochloride
- 300 µM Calcium chloride
- 134 µM Tetrasodium EDTA
- 56.6 µM Boric acid
- 31 µM Iron(III) chloride
- 9 µM Nickel chloride hexahydrate
- 6.2 µM Zinc chloride
- 4 µM Biotin
- 4 µM Sodium selenite
- 3.2 µM Sodium molybdate dihydrate
- 2.7 µM Cobalt(II) chloride hexahydrate
- 1.3 µM Manganese(II) chloride tetrahydrate
- 0.2 µM Copper(II) sulphate

S.3. FTIR Spectroscopy of CO_2 and Ethanol

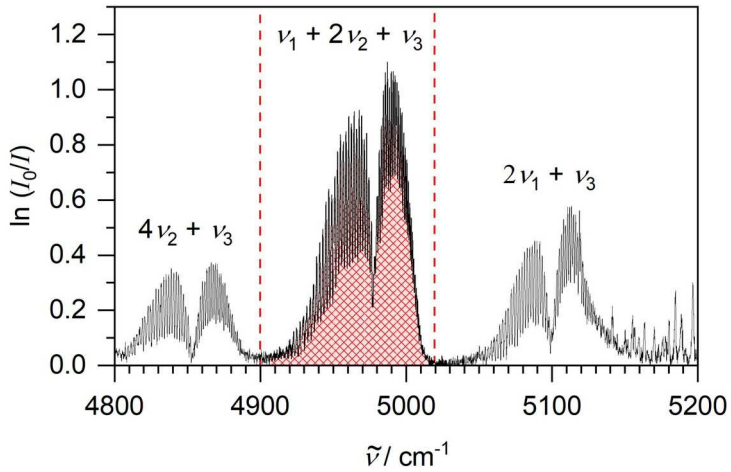

Fig. S2. Experimental White cell FTIR Spectrum of the CO_2 ($2\nu_1+\nu_3$) Fermi triad. The CO_2 partial pressure was 100 mbar calculated from the integral of the shaded $\nu_1+2\nu_2+\nu_3$ band.

Production of CO_2, ethanol and N_2O was quantified by gas-phase FTIR spectroscopy (Mattson Research Series, 0.4 cm^{-1} spectral resolution, 1000 - 7000 cm^{-1} range, liquid N_2 cooled MCT detector) with a home-built multiple-pass absorption White cell [20]. N_2O spectral bands and fitting procedures are described in the main text. Fig. **S2** shows an experimental spectrum of the ($2\nu_1+\nu_3$) Fermi triad of CO_2, corresponding to 100 mbar in 1 atm. The integral of the red-shaded $\nu_1 + 2\nu_2 + \nu_3$ band (4920 - 5015 cm^{-1}, ν_0 = 4978 cm^{-1}) was compared with a reference spectrum taken from the PNNL database to calculate CO_2 partial pressure [21]. PNNL spectra corresponded to 1 ppm-meter of a species and so were scaled to 6 m, the folded pathlength of our White cell.

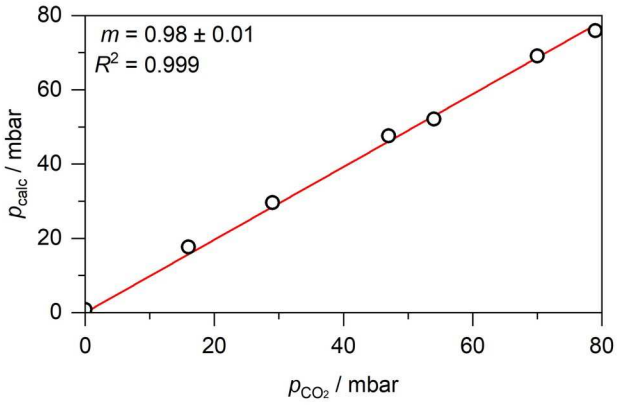

Fig. S3. White cell calibration plot showing the calculated CO_2 partial pressure as a function of CO_2 partial pressure, assuming a folded pathlength of 6 m.

Fig. **S3** shows the excellent linearity between the calculated partial pressures of CO_2 (p_{calc}) and CO_2 in 1 atm air. This confirmed the 6 m folded pathlength of our White cell. Non-linearity was observed at CO_2 partial pressures greater than 100 mbar due to the $\nu_1 + 2\nu_2 + \nu_3$ exceeding a peak absorbance of unity. This was not an issue for our experiments displayed in the main text as CO_2 produced by *E. coli* did not exceed 100 mbar, under our conditions.

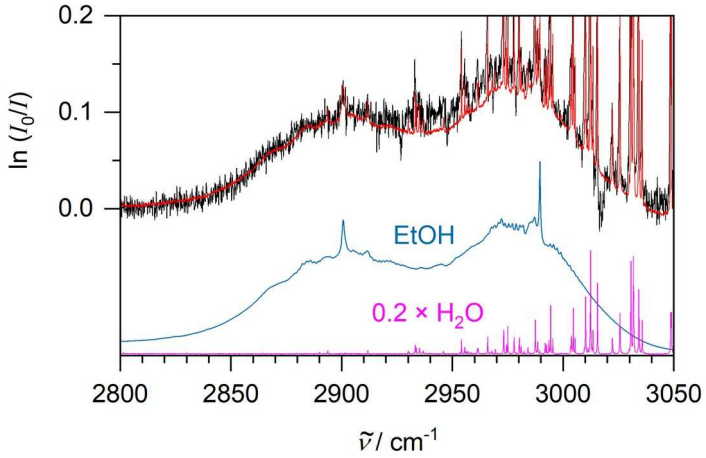

Fig. S4. In black, an experimental White cell FTIR spectrum of 63 ppm ethanol (5.1 mM in solution). In red, the sum of the fitted ethanol and water models shown below the overlaid spectra. The water model is divided by five for clarity due to the intense lines.

Fig. **S4** shows the fitting procedure to obtain ethanol partial pressure. In the C-H stretching region, the broad ethanol peak overlapped with sharp water lines. Using a least-squares fitting routine, model spectra of 1 ppm ethanol and water taken from the PNNL database were fitted to experimental spectra, returning a multiplier equal to the partial pressure of ethanol. Using Henry's law, this partial pressure was converted to concentration in solution.

S.4. Cavity Enhanced Raman Spectroscopy (CERS)

S.4.1. Experimental Details of CERS

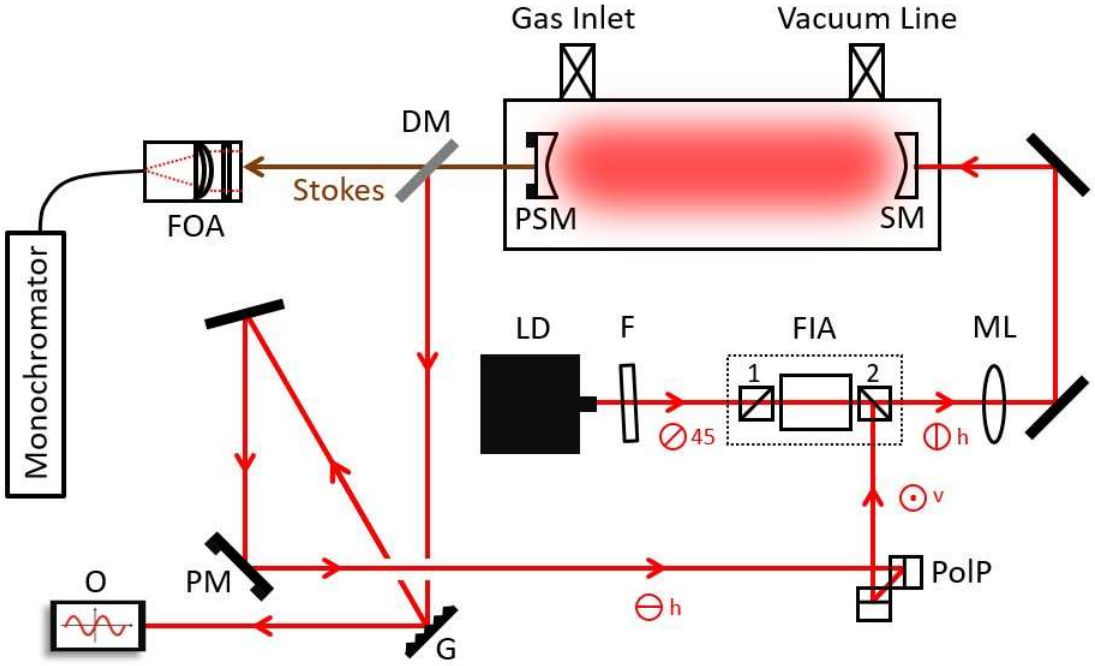

Fig. S5. Scheme of the experimental CERS setup. **DM**, dichroic mirror; **F**, filter; **FIA**, Faraday isolator assembly; **FOA**, fibre optical assembly; **G**, grating; **LD**, laser diode; **ML**, mode matching lens; **O**, oscilloscope; **PM**, mirror on a piezomount; **PolP**, polarization plane turning prism pair; **PSM**, supermirror on a piezomount; **SM**, supermirror.

The experimental CERS setup (Fig. **S5**) has been described before [22–25], but contains several modifications. A 40 mW 636 nm single-mode cw-diode laser (HL63133DG) is coupled *via* a short-pass filter, a Faraday isolator and a mode matching lens into a linear optical cavity composed of two highly reflective mirrors (Newport SuperMirrors, R > 99.99 %). If the laser wavelength matches the cavity length, then an optical resonance builds up optical power inside the cavity by up to 3 orders of magnitude, enhancing the Raman signals. The enhancement can be clearly seen in Fig. **S6** showing a photograph that was taken when the cavity was opened for cleaning. In the present simplified setup, no active mode matching was attempted; the diode laser current was rather modulated periodically to allow periodic mode matching which is then re-enforced by optical feedback. After the cavity, a dichroic mirror separates leftover excitation light from Raman signals which are coupled into a round-to-linear glass fibre bundle (7 x Ø105 µm) and transferred to the monochromator. Remaining excitation light is fed back to the diode for frequency stabilization to match the laser wavelength to the cavity. In the feedback loop there are a grating (G), a piezo-mounted mirror (PM) and a set of 2 prisms (PolP) to change the polarisation from horizontally to vertically polarised. The grating is in 1st order reflection to select just one wavelength of the possible cavity modes, to encourage single mode operation by feedback. The piezo-mirror is to adjust the feedback loop length to the laser wavelength ('phase matching'). In a simplification, we are not using active phase matching but apply a periodic change which will lock the laser periodically to a resonance. In the setup, only one Faraday isolator is used. The original 45° polarised diode laser light will be horizontally polarised after the isolator. To

allow feeding light back to the diode *via* the rejection port of the Faraday isolator, it has to be vertically polarised which is achieved by the prism pair rotating the polarisation.

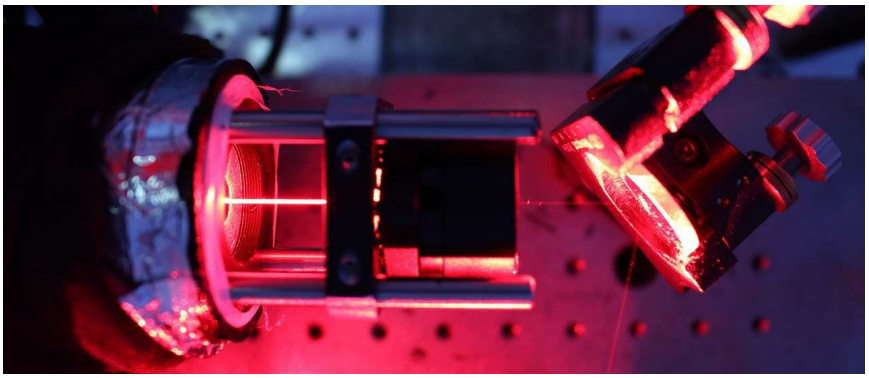

Fig. S6. Photograph taken of the inside of the cavity while open for cleaning, clearly showing the power enhancement of the red laser beam inside the cavity.

S.4.2. Spectral Fitting Procedures and Calibration Plots

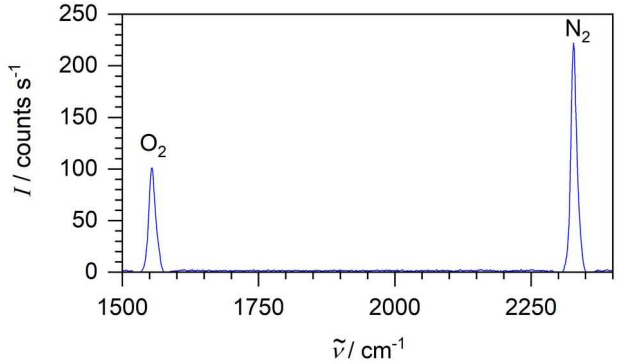

Fig. S7. CERS spectrum of 1 atm air (210 mbar O_2 and 790 mbar N_2).

Fig. **S7** shows a CERS spectrum of air, with the *Q*-branches of the O_2 and N_2 vibrational fundamentals visible. Fig. **S8** shows a CERS spectrum of 140 mbar each of H_2 and CO_2, taken during a bacterial anaerobic fermentation experiment.

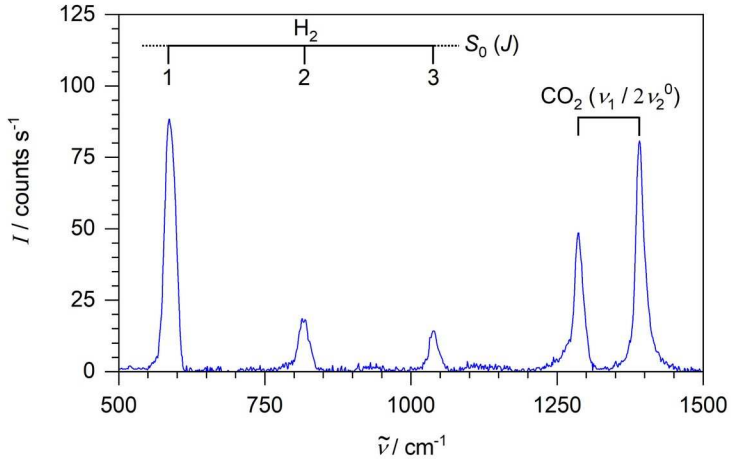

Fig. S8. CERS spectrum of H_2 and CO_2 (140 mbar of each).

The area of the *S*(1) rotational peak of H_2 was divided by the area of the *Q*-branch of N_2 (corresponding to 1 atm in anaerobic experiments) in order to obtain H_2 partial pressures after a calibration. Using known partial gas pressures, a calibration was made for H_2 showing excellent

linearity, see Fig. **S9**. A similar procedure has been applied to CO_2; the calibration also shows excellent linearity, see Fig. **S9**.

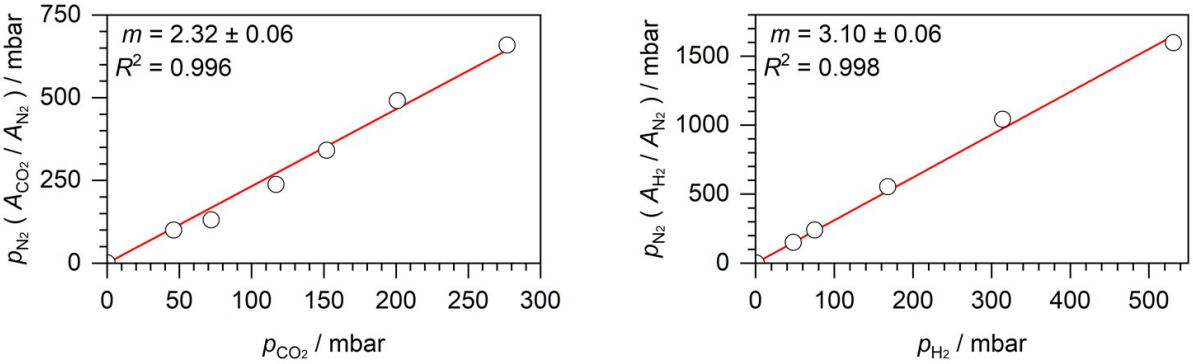

Fig. S9. CO_2 and H_2 calibration plots.

S.5. Liquid Phase Raman Spectroscopy

S.5.1. Experimental Details of the Home-built Raman Spectrometer

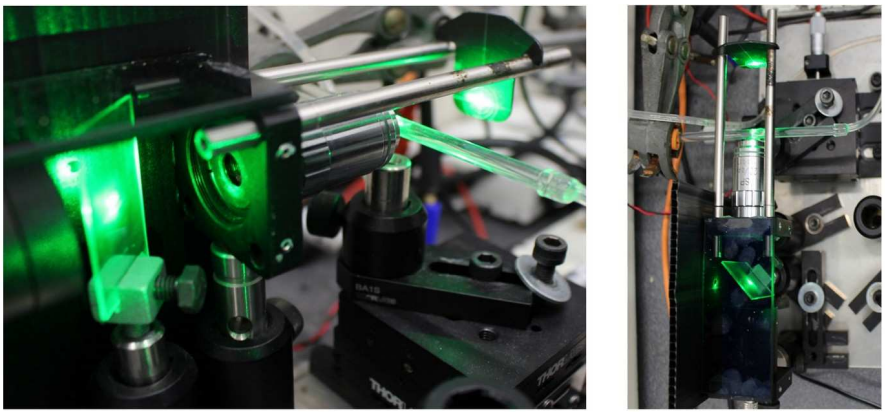

Fig. S10. Photographs of the home-built spectrometer set-up, showing the laser beam path through the mirror and the microscope objective to the sample. Left: side view; right: top view.

The home-built Raman spectrometer was first described in ref. [26] and modified later as described in refs. [20, 27]; key components of the monochromator and the camera have been described in refs [22, 23]. Briefly, a frequency doubled Nd:YAG laser, 532.2 nm, 20 mW (Lasos, GL3dT) emits green excitation light that is turned by 90° by a small mirror and coupled into a microscope objective. The small mirror was a 2 mm × 3 mm oval film deposited in the centre of a glass slide so as not to take away too much of the Raman backscattered light. The microscope objective is a 20x, 0.50 NA achromatic objective (OptoSigma, 028-0220) with a large clear aperture (8.2 mm). The objective focused the laser light very tightly at 2 mm distance from the objective front into the glass tube, as well as collimating the resulting Raman backscattered light. The sample volume is essentially the focus volume with an estimated spatial resolution below 100 µm. The backscattered light passed through the glass slide and was coupled into a lens and transmitted to the monochromator (Shamrock SR-750-A) equipped with 1200 l/mm grating, 750 nm blaze, and CCD camera (Andor i-Dus DU420A-OE at –80 °C). The grating provided a 880 cm-1 spectral range at about 0.8 cm-1 resolution. After wavenumber calibration, Raman peak position accuracy is estimated to be ± 3 cm-1 .

Raman reference spectra were obtained in borosilicate NMR test tubes. A scheme of the Raman setup is part of Fig. 2 in the main text. In addition, see Fig. **S10** for two photos of the Raman spectrometer.

S.5.2. Spectral Fitting Procedures and Calibration Plots

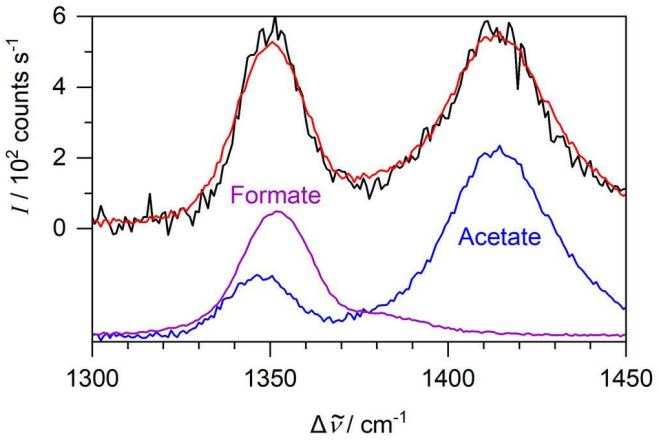

Fig. S11. In black, an experimental Raman spectrum of M9 medium containing 30 mM acetate and 10 mM formate excreted by *E. coli*. In red, the sum of the fitted acetate and formate models shown below the overlaid spectra.

As described in the main text, experimental liquid Raman spectra were fitted with the sum of model Raman spectra of pure compounds of known concentration and a linear baseline. Fig. 3 in the main text shows an example fitting procedure for NO_3^-, glucose, $H_2PO_4^-$ and HPO_4^{2-} at 825 - 1200 cm^{-1}. Fig. **S11** shows an example fit for the other species we analyse by liquid phase Raman spectroscopy, acetate and formate between 1300 - 1450 cm^{-1}, as first described in ref. [20].

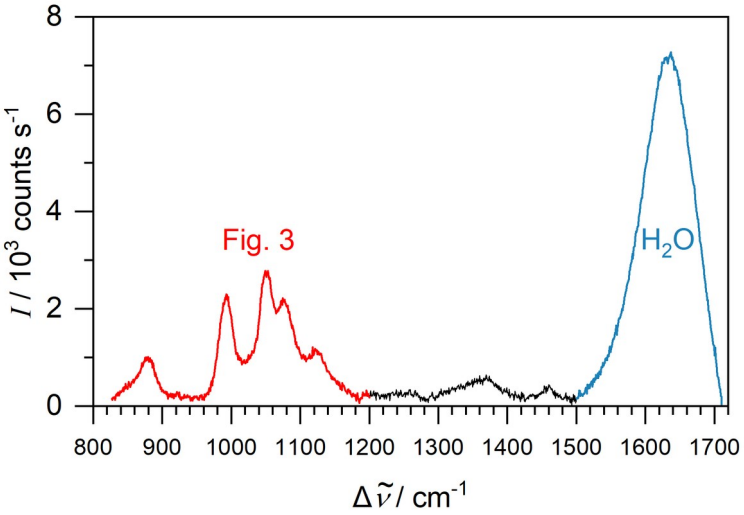

Fig. S12. The entire experimental Raman spectrum of M9 medium supplemented with 10 mM $K^{15}NO_3$ and 30 mM glucose.The water bending vibration is highlighted in blue. See the main text for Fig. 3.

The least-squares fitting procedures returned multipliers *x* that were normalised by dividing by the water area peak (bending vibration of the water solvent at 1630 cm^{-1}) to give *x*'; this normalisation was particularly relevant for our biological samples which became turbid with time. In the normalisation, the water peak was fitted by a Gaussian contour centered at 1630 cm^{-1} with FWHM

of 80 cm^{-1}. Normalisation assumed that the area of this Gaussian was the same in all solution Raman spectra because water concentrations remained the same. Fig. **S12** shows the water peak as well as the entire spectral range (830 - 1710 cm^{-1}) of a typical solution Raman spectrum. The part of the spectrum coloured red is displayed in the main text in Fig. 3.

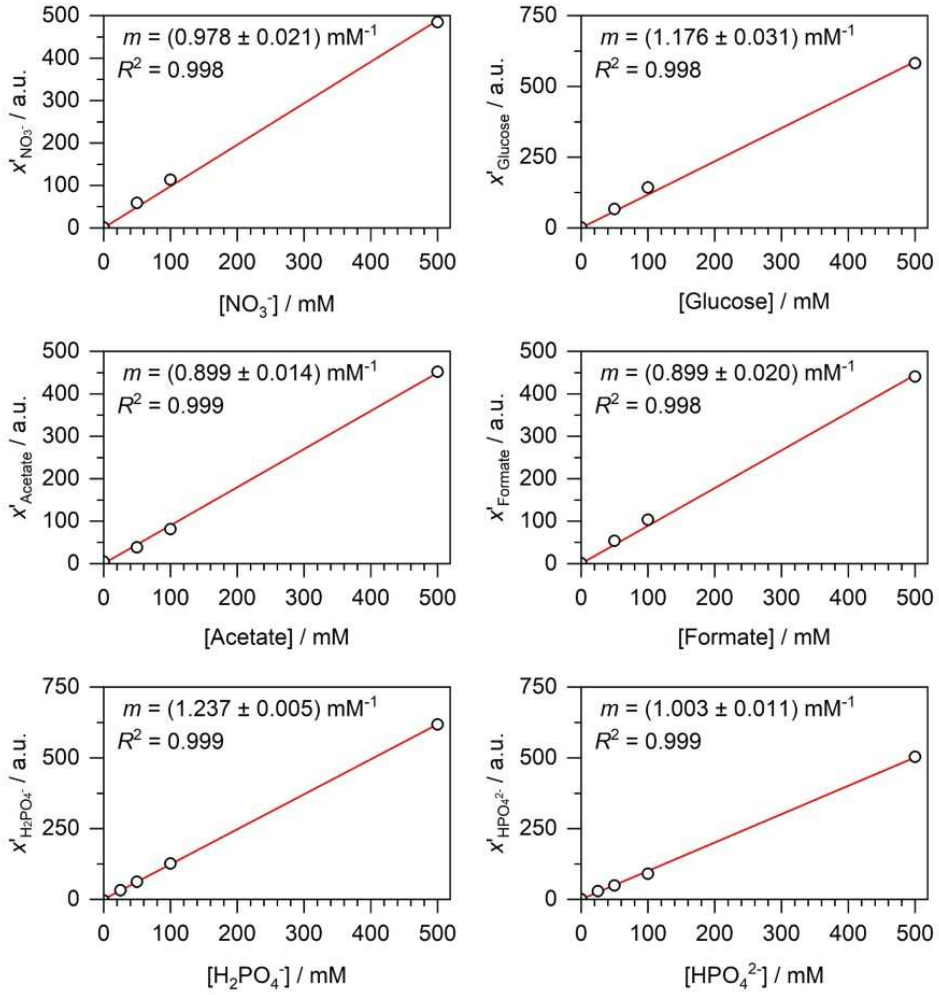

Fig. S13. Calibration plots of normalized Raman signals *x*' (in a.u.) *versus* concentration in solution for NO_3^-, glucose, acetate, formate, $H_2PO_4^-$ and HPO_4^{2-}; with linear fit lines, slopes *m* and R^2 values.

The normalized x' provides the concentration of the compound in comparison with the known concentration of the pure compound used as the model for the fit. This procedure was validated by calibration plots shown in Fig. **S13** where the concentrations of calibration solutions were determined as described above and compared with the nominal concentrations. Excellent linearity (as shown by the R^2 value) and a good dynamic range are demonstrated in all cases. m denotes the slope of the calibration curves. Error bars, as represented by the standard deviation of repeat measurements, are approximately the size of the symbols used or smaller and are therefore not included in the calibration plots.

S.6. Analysis of Bacterial Culture Samples

S.6.1. Nitrite Colorimetry

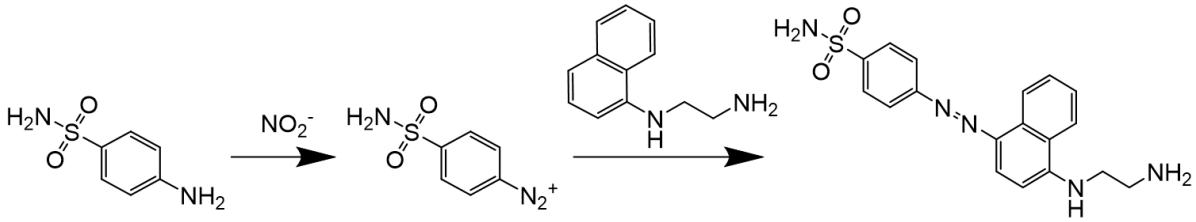

Scheme S1. The two subsequent reactions of the Griess test.

Scheme **S1** shows the two subsequent reactions of the Greiss test. First NO_2^- reacts with sulfanilamide forming a diazonium salt which then reacts in an azo coupling reaction with N-(1-napthyl)ethylenediamine forming a pink azo dye. The pink colour is shown in Fig. **S14**.

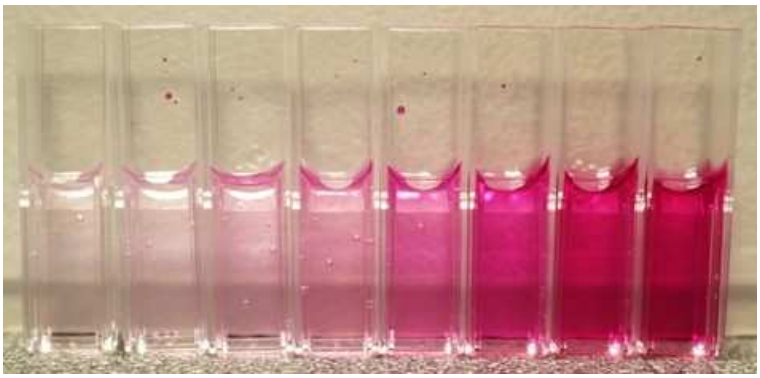

Fig. S14. The pink azo dye formed by the Griess test for NO_2^-.

By using a spectrophotometer, NO_2^- can be quantitatively determined by measuring the absorbance at 520 nm, as shown by the calibration plot in Fig. **S15**.

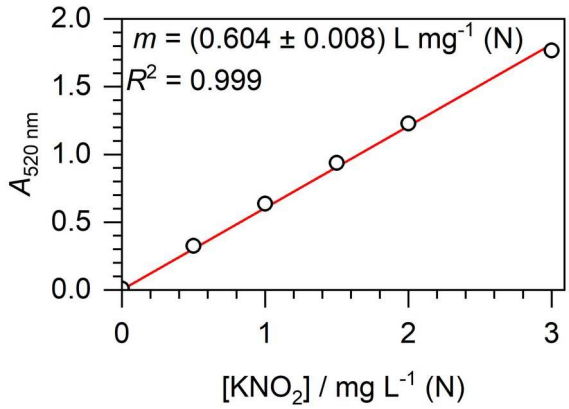

Fig. S15. NO_2^- colorimetry calibration plot.

S.6.2. $^{14}N/^{15}N$-Ammonium Analysis

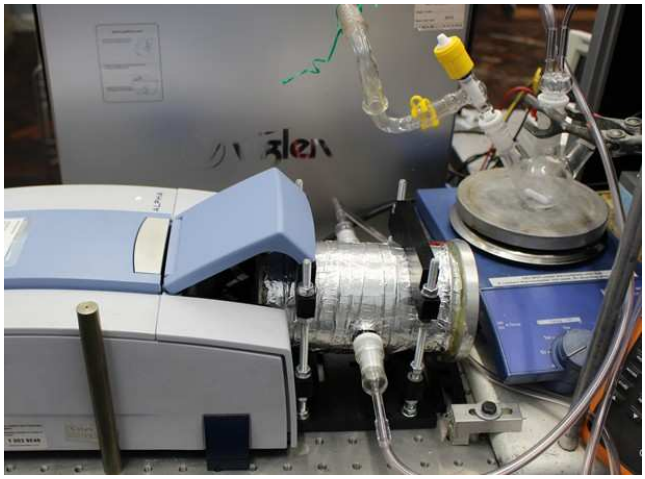

Fig. S16. The White cell (2.8 m folded pathlength) FTIR and flask setup for analysing $^{14}NH_3$ and $^{15}NH_3$.

For $^{14}N/^{15}N$ ammonium analysis of samples, 2 mL 1 M NaOH was added to 0.6 mL of sample to release ammonia gas in a flask connected to our second FTIR set-up (Bruker Alpha FTIR, 0.8 cm^{-1} spectral resolution, 350 - 7000 cm^{-1} range) also with a home-built multiple-pass absorption White cell (2.8 m pathlength), shown in Fig. **S16**. The gases were cycled using a peristaltic pump (4.5 L/h) and the solution was stirred rapidly. Spectra were recorded every 5 minutes with around 30 minutes needed before ammonia concentration peaked in the headspace.

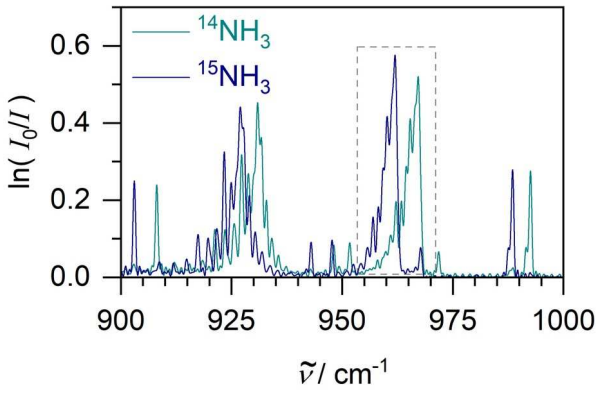

Fig. S17. Experimental White cell FTIR spectra of $^{14}NH_3$ (cyan) and $^{15}NH_3$ (dark blue) gases, each corresponding to 20 mM NH_4^+ in solution. The grey dashed box indicates the ν_2 *Q*-branch fitted for NH_3 analysis.

Fig. **S17** shows typical experimental spectra of $^{14}NH_3$ (black) and $^{15}NH_3$ (red) gases, both corresponding to 20 mM ammonium. The two *Q*-branches of ammonia's ν_2 N-H wagging fundamental are visible, it is centred around 950 cm^{-1} for $^{14}NH_3$. Two *Q*-branches are observed due to the inversion doubling phenomenon exhibited by trigonal pyramidal molecules like ammonia. The ν_2 *P*- and *R*- branches extend over 700 - 1200 cm^{-1}, outside the range displayed for the spectra. The ν_2 band is the strongest in ammonia's IR spectrum and free from CO_2 and water lines and is commonly used for FTIR analysis of $^{14}N/^{15}N$ ammonia. We observed the higher energy *Q*-branch, highlighted by

a dashed box for the prior spectra, to be the most intense ammonia spectral feature so it was utilised for analysis. A self-written computer programme implements the least-squares fit of the 955 - 970 cm^{-1} region of an experimental FTIR spectrum to the sum of scaled $^{14}NH_3$ and $^{15}NH_3$ model spectra and a linear baseline.

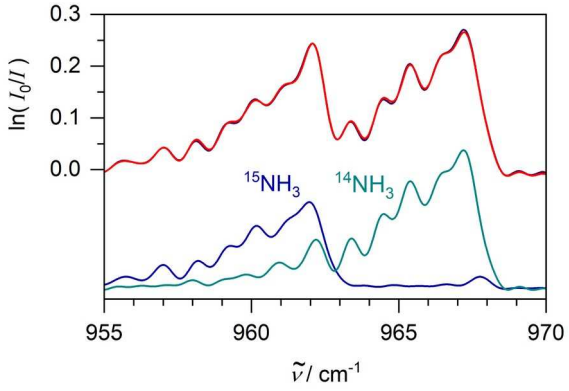

Fig. S18. In black, an experimental White cell FTIR spectrum of $^{14}NH_3$ and $^{15}NH_3$ gases corresponding to 12.5 mM $^{14}NH_4^+$ and 8.25 mM $^{15}NH_4^+$. In red, the sum of the fitted $^{14}NH_3$ and $^{15}NH_3$ models shown below the overlaid spectra.

Fig. **S18** is an example least-squares fit for $^{14}NH_3$ and $^{15}NH_3$. Calibration plots were constructed (shown below in Fig. **S19**) to convert the multipliers of the model spectra (*x*') into concentrations. The model NH_3 spectra were constructed from experimental spectra.

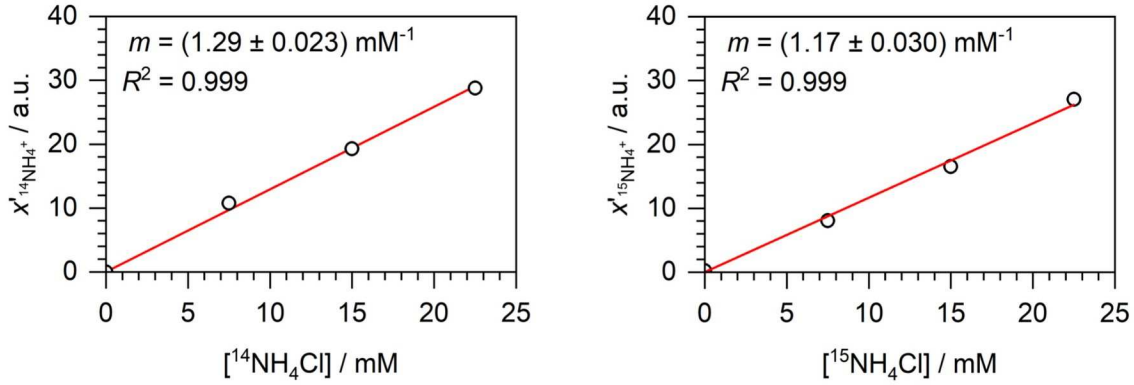

Fig. S19. Calibration plots for $^{14}NH_3$ and $^{15}NH_3$.

Under our conditions, we obtained a dynamic range up to 22.5 mM and a noise equivalent detection limit (1 σ) of 0.13 mM. This was suitable for our bacterial culture samples containing 18 mM $^{14}NH_4^+$ and 10 mM $^{15}NO_3^-$ at the start. $^{14}NH_4^+$ concentrations can only decrease due to biomass synthesis and $^{15}NH_4^+$ concentrations produced cannot exceed that of the 10 mM $^{15}NO_3^-$ supplied.

S.7. References

1. Stewart, V. Nitrate respiration in relation to facultative metabolism in enterobacteria. *Microbiol. Rev.* **1988**, *52*, 190-232, https://doi.org/10.1128/mr.52.2.190-232.1988
2. Bonnefoy, V.; Demoss, J. A. Nitrate reductases in *Escherichia coli*. *Antonie van Leeuwenhoek*. **1994**, *66*, 47-56, https://doi.org/10.1007/BF00871632
3. Stewart, V.; Lu, Y.; Darwin, A. J. Periplasmic nitrate reductase (NapABC enzyme) supports anaerobic respiration by *Escherichia coli* K-12. *J. Bacteriol.* **2002**, *184*, 1314-1323, https://doi.org/10.1128/JB.184.5.1314-1323.2002
4. Wang, H.; Tseng, C. P.; Gunsalus, R. P. The *napF* and *narG* Nitrate Reductase Operons in *Escherichia coli* Are Differentially Expressed in Response to Submicromolar Concentrations of Nitrate but Not Nitrite. *J. Bacteriol.* **1999**, *181*, 5303-5308, https://doi.org/10.1128/JB.181.17.5303-5308.1999
5. Cole, J. Nitrate reduction to ammonia by enteric bacteria: redundancy, or a strategy for survival during oxygen starvation? *FEMS Microbiol. Lett.* **1996**, *136*, 1-11, https://doi.org/10.1016/0378-1097(95)00480-7
6. Chang, L.; Wei, L. I.; Audia, J. P.; Morton, R. A.; Schellhorn, H. E. Expression of the *Escherichia coli* NRZ nitrate reductase is highly growth phase dependent and is controlled by RpoS, the alternative vegetative sigma factor. *Mol. Microbiol.* **2002**, *34*, 756-766, https://doi.org/10.1046/j.1365-2958.1999.01637.x
7. Wang, H.; Gunsalus, R. P. The *nrfA* and *nirB* Nitrite Reductase Operons in *Escherichia coli* Are Expressed Differently in Response to Nitrate than to Nitrite. *Genet. Mol. Biol.* **2000**, *182*, 5813-5822, https://doi.org/10.1128/jb.182.20.5813-5822.2000
8. Smith, M. S. Nitrous oxide production by *Escherichia coli* is correlated with nitrate reductase activity. *Appl. Environ. Microbiol.* **1983**, *45*, 1545-1547, https://doi.org/10.1128/AEM.45.5.1545-1547.1983
9. Metheringham, R.; Cole, J. A. A reassessment of the genetic determinants, the effect of growth conditions and the availability of an electron donor on the nitrosating activity of *Escherichia coli* K-12. *Microbiol.* **1997**, *143*, 2647-2656, https://doi.org/10.1099/00221287-143-8-2647
10. Gilberthorpe, N. J.; Poole, R. K. Nitric oxide homeostasis in *Salmonella typhimurium*. *J. Biol. Chem.* **2008**, *283*, 11146-11154, https://doi.org/10.1074/jbc.M708019200
11. Vine, C. E.; Purewal, S. K.; Cole, J. A. NsrR-dependent method for detecting nitric oxide accumulation in the *Escherichia coli* cytoplasm and enzymes involved in NO production. *FEMS Microbiol. Lett.* **2011**, *325*, 108-114, https://doi.org/10.1111/j.1574-6968.2011.02385.x
12. Vine, C. E.; Cole, J. A. Nitrosative stress in *Escherichia coli*: reduction of nitric oxide. *Biochem. Soc. Trans.* **2011**, *39*, 213-215, https://doi.org/10.1042/BST0390213
13. Corker, H.; Poole, R. K. Nitric Oxide Formation by *Escherichia coli*: Dependence On Nitrite Reductase, The NO-Sensing Regulator Fnr, and Flavohemoglobin Hmp. *J. Biol. Chem.* **2003**, *278*, 31584-31592, https://doi.org/10.1074/jbc.M303282200
14. Gardner, A. M.; Helmick, R. A.; Gardner, P. R. Flavorubredoxin, an Inducible Catalyst for Nitric Oxide Reduction and Detoxification in *Escherichia coli*. *J. Biol. Chem.* **2002**, *277*, 8172-8177, https://doi.org/10.1074/jbc.M110471200
15. Wang, J.; Vine, C. E.; Balasiny, B. K.; Rizk, J.; Bradley, C. L.; Tinajero-Trejo, M.; Poole, R. K.; Bergaust, L. L.; Bakken, L. R.; Coole, J. A. The role of the hybrid cluster protein, Hcp and its reductase, Hcr, in high affinity nitric oxide reduction that protects anaerobic cultures of *Escherichia coli* against nitrosative stress. *Mol. Microbiol.* **2016**, *100*, 877-892, https://doi.org/10.1111/mmi.13356

16. Weiss, B. Evidence for Mutagenesis by Nitric Oxide during Nitrate Metabolism in *Escherichia coli*. *J. Bacteriol.* **2006**, *188*, 829-833, https://doi.org/10.1128/JB.188.3.829-833.2006
17. Poock, S. R.; Leach, E. R.; Moir, J. W. B.; Cole, J. A.; Richardson, D. J. Respiratory Detoxification of Nitric Oxide by the Cytochrome *c* Nitrite Reductase of *Escherichia coli*. *J. Biol. Chem.* **2002**, *277*, 23664-23669, https://doi.org/10.1074/jbc.M200731200
18. Kim, S. O.; Orii, Y.; Lloyd, D.; Hughes, M. N.; Poole, R. K. Anoxic function for the *Escherichia coli* flavohaemoglobin (Hmp): reversible binding of nitric oxide and reduction to nitrous oxide. *FEBS Lett.* **1999**, *445*, 389-394, https://doi.org/10.1016/S0014-5793(99)00157-X
19. Kaldorf, M.; Linne von Berg, K. H.; Meier, U.; Servos, U.; Bothe, H. The reduction of nitrous oxide to dinitrogen by *Escherichia coli*. *Arch. Microbiol.* **1993**, *160*, 432-439, https://doi.org/10.1007/BF00245303
20. Metcalfe, G. D.; Smith, T. W.; Hippler, M. On-line analysis and in situ pH monitoring of mixed acid fermentation by *Escherichia coli* using combined FTIR and Raman techniques. *Anal. Bioanal. Chem.* **2020**, *412*, 7303-7319, https://doi.org/10.1007/s00216-020-02865-5
21. Sharpe, S. W.; Johnson, T. J.; Sams, R. L.; Chu, P. M.; Rhoderick, G. C.; Johnson, P. A. Gas-Phase Databases for Quantitative Infrared Spectroscopy. *Appl. Spectrosc.* **2004**, *58*, 1452-1461, https://doi.org/10.1366/0003702042641281
22. Salter, R.; Chu, J.; Hippler, M. Cavity-enhanced Raman spectroscopy with optical feedback cw diode lasers for gas phase analysis and spectroscopy. *Analyst.* **2012**, *137*, 4669-4676, https://doi.org/10.1039/c2an35722d
23. Hippler, M. Cavity-Enhanced Raman Spectroscopy of Natural Gas with Optical Feedback cw-Diode Lasers. *Anal. Chem.* **2015**, *87*, 7803-7809, https://doi.org/10.1021/acs.analchem.5b01462
24. Smith, T. W.; Hippler, M. Cavity-Enhanced Raman Spectroscopy in the Biosciences: *In situ*, Multicomponent, and Isotope Selective Gas Measurements To Study Hydrogen Production and Consumption by *Escherichia coli*. *Anal. Chem.* **2017**, *89*, 2147-2154, https://doi.org/10.1021/acs.analchem.6b04924
25. Metcalfe, G. D.; Alahmari, S.; Smith, T. W.; Hippler, M. Cavity-Enhanced Raman and Helmholtz Resonator Photoacoustic Spectroscopy to Monitor the Mixed Sugar Metabolism of *E. coli*. *Anal. Chem.* **2019**, *91*, 13096-13104, https://doi.org/10.1021/acs.analchem.9b03284
26. Mohr, C.; Spencer, C. L.; Hippler, M. Inexpensive Raman Spectrometer for Undergraduate and Graduate Experiments and Research. *J. Chem. Educ.* **2010**, *87*, 326-330, https://doi.org/10.1021/ed800081t
27. Ryabenkova, Y.; Jadav, N.; Conte, M.; Hippler, M.; Reeves-McLaren, N.; Coates, P. D.; Twigg, P.; Paradkar, A. Mechanisms of Hydrogen-Bonded Complex Formation between Ibuprofen and Nanocrystalline Hydroxyapatite. *Langmuir.* **2017**, *33*, 2965-2976, https://doi.org/10.1021/acs.langmuir.6b04510